A&A 365, 440–464 (2001)
DOI: 10.1051/0004-6361:20000072


Astronomy & Astrophysics

# The circumstellar environment of low-mass protostars: A millimeter continuum mapping survey⋆

F. Motte[1,2,⋆⋆] and P. André[2]

[1] Max-Planck-Institut für Radioastronomie, Auf dem Hügel 69, 53121 Bonn, Germany
[2] CEA, DSM, DAPNIA, Service d'Astrophysique, CE Saclay, 91191 Gif-sur-Yvette Cedex, France

Received 6 June 2000 / Accepted 5 September 2000

**Abstract.** We present a complete 1.3 mm continuum mapping survey of the embedded young stellar objects (YSOs) in the Taurus molecular cloud. We have also imaged several isolated Bok globules, as well as protostellar objects in the Perseus cluster. Our maps, taken with the IRAM 30 m telescope and the MPIfR bolometer arrays, are sensitive to the column density structure of the sources on spatial scales ranging from 1 500–5 000 AU to $>$ 15 000–50 000 AU. For the protostellar envelopes mapped in Taurus, the results are roughly consistent with the predictions of the self-similar inside-out collapse model of Shu and collaborators. The envelopes observed in Bok globules are also qualitatively consistent with these predictions, providing the effects of magnetic pressure are included in the model. By contrast, the envelopes of Class 0 protostars in Perseus have finite radii $\lesssim$ 10 000 AU and are a factor of 3 to 12 denser than is predicted by the standard model. In cluster-forming regions, individual protostellar collapse thus appears to be induced in compact condensations resembling more finite-sized Bonnor-Ebert condensations than singular isothermal spheres. Accordingly, the beginning of protostellar evolution is suggested to be more violent, with larger accretion rates, in protoclusters compared to regions of distributed star formation like Taurus. Follow-up line observations of the envelopes' velocity fields are required to confirm this suggestion. We also find that roughly half of the Class I infrared sources of Taurus are either at the very end of the main accretion phase or already in the pre-main sequence phase. These sources are surrounded by only remnant, finite-sized envelopes ($M_{\rm env}^{4200\ {\rm AU}} \lesssim 0.01\ M_\odot$ and $R_{\rm out} \lesssim 1\,500$ AU). Lastly, our 1.3 mm continuum images reveal the presence of new candidate pre-stellar condensations and/or Class 0 protostars in the close environment of 8 Taurus Class I YSOs, 2 Bok globules, and 3 Perseus protostars.

**Key words.** stars: formation – stars: circumstellar matter – ISM: clouds – ISM: structure – ISM: dust

## 1. Introduction: Testing the predictions of collapse models

In the course of early stellar evolution, one expects progressive condensation of the circumstellar material surrounding young stellar objects (YSOs) from "cloud-core" sizes (∼0.1 pc $\gtrsim$ 10 000 AU) to solar-system sizes (∼10–100 AU). Therefore, sensitive, high-angular-resolution maps of the circumstellar environment of YSOs such as those resulting from observations of optically thin dust continuum emission on large (sub)millimeter radiotelescopes, can potentially provide crucial tests of our theoretical ideas on star formation. In this paper, we present an extensive 1.3 mm continuum mapping study of a large sample of nearby protostellar dense cores in order to set constraints on their density structure. Below, we give a brief overview of existing collapse models and summarize the results of previous inconclusive observations.

In the "standard" theory of spontaneous isolated star formation (e.g. Shu et al. 1987), low-mass stars form from dense cloud cores which have reached, in a quasi-static fashion, the $\rho(r) \propto r^{-2}$ density distribution of a singular isothermal spheroid (SIS) or toroid (cf. Li & Shu 1996, 1997). The collapse of such initially hydrostatic but unstable spheroids proceeds from the inside out, with production of a central "protostar" surrounded by an infalling envelope (e.g. Shu et al. 1987). At any given time, the infall envelope is bounded by the front of a collapse expansion wave which propagates outward at the isothermal sound speed, $a_{\rm s}$. Outside the time-dependent radius $r_0 = a_{\rm s}\,t$ of the infalling envelope, the cloud core is at rest and retains its initial $\rho(r) \propto r^{-2}$ density structure. Inside $r_0$, the material is nearly in free-fall and the density asymptotically

*Send offprint requests to*: F. Motte,
e-mail: motte@submm.caltech.edu

⋆ Figures 9 to 12 are only available in electronic form at http://www.edpsciences.org

⋆⋆ Present address: California Institute of Technology, MS 320-47, Pasadena, CA 91125, USA

approaches a $\rho(r) \propto r^{-1.5}$ power-law[1]. This protostellar model starting from SIS initial conditions has been widely used in the past, partly because it is based on a relatively simple, semi-analytical similarity solution for the collapse (Shu 1977), allowing rotation and magnetic fields to be treated as perturbations (e.g. Terebey et al. 1984; Galli & Shu 1993).

Other collapse models exist that adopt different initial conditions. Whitworth & Summers (1985) have shown that there is a two-dimensional continuum of similarity solutions to the problem of isothermal spherical collapse. In this continuum, the well-known solutions proposed by Shu (1977) and Larson (1969), Penston (1969) represent two extreme limits. All isothermal similarity solutions share a universal evolutionary pattern. At early times ($t < 0$), a compression wave (initiated by, e.g., an external disturbance) propagates inward at the sound speed, leaving behind it a $\rho(r) \propto r^{-2}$ density profile. At $t = 0$, the compression wave reaches the center and a point mass forms which subsequently grows by accretion. At later times ($t > 0$), this wave is reflected into a rarefaction or expansion wave, propagating outward (also at the sound speed) through the infalling gas, and leaving behind it a free-fall $\rho(r) \propto r^{-1.5}$ density distribution. Several features of the standard model described above are thus in fact general. The various solutions can be distinguished by the *absolute* values of the density and velocity at $t \sim 0$. In particular, the Shu (1977) solution has $\rho(r) = ({a_s}^2/2\pi G)\ r^{-2}$ and is static ($v = 0$) at $t = 0$, while the Larson-Penston (1969) solution is ∼4.4 times denser and far from equilibrium ($v \approx -3.3\ a_s$). Apart from their simplicity, the great interest of these similarity solutions is that they represent asymptotes in various regimes of more complicated flows.

In practice, however, the initial conditions for fast protostellar collapse may not be self-similar and may involve a density profile that is flat at small radii (e.g. Ward-Thompson et al. 1994; André et al. 1996 – hereafter AWM96) and bounded or sharp-edged at some outer radius $R_{\rm out}$ (e.g. Motte et al. 1998 – hereafter MAN98; Bacmann et al. 2000) like a finite-sized Bonnor-Ebert isothermal sphere (e.g. Bonnor 1956). A number of recent numerical (magneto)hydrodynamic simulations or simplified analytical calculations attempt to describe the collapse in such a situation, either in the absence (e.g. Foster & Chevalier 1993; Henriksen et al. 1997 – HAB97; Masunaga et al. 1998) or in the presence (e.g. Tomisaka 1996; Basu 1997; Safier et al. 1997; Li 1998; Ciolek & Königl 1998) of magnetic fields. These studies find that supersonic infall velocities generally develop before point mass formation at $t = 0$. The Larson-Penston similarity solution is found to describe the collapse quite satisfactorily near $t = 0$ (at least for small radii), but the Shu solution is more adequate at intermediate $t \geq 0$ times, before the expansion wave reaches the edge of the initial, pre-collapse dense core.

In order to fully distinguish between collapse models, observations of both the density and the velocity profile of protostellar dense cores are in principle required. Since the density structure is much easier to measure, we focus on this type of observational constraints as a first step. Most previous relevant studies had only the spatial resolution to constrain the extreme outer parts of star-forming cloud cores (from ∼0.1 pc ∼ 20 000 AU to ∼1 pc – e.g., Loren et al. 1983; Cernicharo et al. 1985; Casali 1986; Davidson 1987; Yun & Clemens 1991 – hereafter YC91). On smaller spatial scales ($\lesssim$ 20 000 AU), only a few protostellar envelopes have been investigated in detail up to now (e.g., Walker et al. 1990; Ladd et al. 1991; Butner et al. 1991; Barsony & Chandler 1993; Chandler et al. 1998). These studies have yielded contradictory, inconclusive results, i.e., radial density profiles of the type $\rho(r) \propto r^{-p}$ with $p$ ranging from 0.5 (e.g. Barsony & Chandler 1993) to 3 (e.g. YC91). A more comprehensive investigation on a broad, homogeneous sample of protostellar dense cores on spatial scales < 0.1 pc is thus clearly called for to make progress and draw more definite conclusions.

The present paper discusses the results of a systematic 1.3 mm dust continuum mapping investigation conducted at an angular resolution of 11″ with the IRAM 30 m telescope. These 1.3 mm observations probe the column density structure of protostellar envelopes on spatial scales from $r \sim$ 1 500–5 000 AU to $r \sim$ 17 000–55 000 AU in nearby star-forming regions (at $d =$ 140–460 pc). Several related studies have been recently carried out at 850 $\mu$m with SCUBA on JCMT (Chandler & Richer 2000; Hogerheijde & Sandell 2000; Shirley et al. 2000). Our work differs from these studies in that our source sample is larger and much more comprehensive; in particular, it includes *all* of the known embedded YSOs in a single star-forming cloud, namely Taurus (cf. Sect. 2.1).

The layout of the paper is as follows. In Sect. 2, we present our millimeter continuum mapping survey of the Taurus embedded YSOs, along with several isolated IRAS globules, and some clustered protostars in Perseus. The results and analysis of the density structure of protostellar envelopes are given in Sects. 3 and 4, respectively. Section 5 presents a careful comparison of the protostellar density structure observed in isolated and clustered regions with theoretical predictions of protostellar collapse models. An evolutionary scenario is also given for the Taurus embedded YSOs, believed to be prototypical isolated sources. Our conclusions are summarized in Sect. 6.

## 2. Millimeter continuum observations

### 2.1. Source sample and classification

The original goal of our bolometer observations was to make a complete, homogeneous survey for 1.3 mm continuum emission in the embedded YSOs known in the

[1] There is, however, a transition region just inside the expansion wavefront where the density gradient is flatter and closer to $\rho(r) \propto r^{-1}$.

Taurus-Auriga molecular cloud complex (e.g., Myers et al. 1987 – M 87 –; Kenyon et al. 1990 – KHSS90 –; Kenyon & Hartmann 1993; Tamura et al. 1991). Our Taurus subsample thus comprises 26 YSOs which have all been classified as Class I sources, hence candidate protostars (see below), on the basis of their infrared spectral energy distributions (SEDs) (e.g. M 87, KHSS90, and Table 2). It also includes the Class 0 object IRAM 04191+1523 (IRAM 04191 for short) which was discovered in the course of this 1.3 mm continuum survey and is presently undetected shortward of 60 $\mu$m (see André et al. 1999 – hereafter AMB99).

The Taurus cloud has a relatively low spatial density of YSOs and is believed to be representative of the isolated or distributed mode of low-mass star formation (e.g. Gómez et al. 1993). In this case, it has been argued that stars form as a result of the self-initiated collapse of isolated dense cores, possibly driven by ambipolar diffusion (e.g. Myers 1987; Lizano & Shu 1989; Mouschovias 1991; although see Hartmann 2000). Accordingly, Taurus-Auriga may be the nearest ($d$ = 140 pc) and best example of a major star-forming region where the standard self-similar theory of isolated protostars (see Sect. 1) should apply to a good approximation.

In order to investigate the possible influence of environmental effects on the structure of protostellar envelopes, we then enlarged our initial Taurus sample by including several Bok globules detected by IRAS at $d$ = 160–460 pc (e.g. Benson & Myers 1989; Yun & Clemens 1992), as well as embedded YSOs in the Perseus molecular cloud complex at $d \sim 300$ pc (e.g. Bachiller et al. 1991a,b). The Bok globules are small isolated molecular clouds, not clearly associated with any star-forming complex (e.g. Clemens & Barvainis 1988; Lee & Myers 1999), that should also resemble the predictions of the standard protostellar model. By contrast, protostellar evolution in cluster-forming clouds such as Perseus and $\rho$ Ophiuchi is likely to depart significantly from scale-free descriptions (e.g. MAN98; see also Sect. 5 below).

Table 1 lists the most common names of each source in the literature (Col. 1), the abbreviated name adopted in this paper (Col. 2), the source 1950 equatorial coordinates (Cols. 3 and 4, based on the reference listed in Col. 8), along with its adopted distance (Col. 5), bolometric temperature (Col. 6), and bolometric luminosity (Col. 7, based on the reference listed in Col. 9). In total, we took 1.3 mm continuum maps toward 49 embedded YSOs, which are broken down into 4 Class II, 30 Class I, and 15 Class 0 sources.

In this classification, Class 0 sources, distinguished by large submillimeter to bolometric luminosity ratios and self-embedded in massive circumstellar envelopes, are believed to be young protostars at the beginning of the main accretion phase (André et al. 1993, 2000 – hereafter AWB93, AWB2000). Class I sources, characterized by rising SEDs from $\sim$2 $\mu$m to $\sim$25−100 $\mu$m, are interpreted as more evolved protostars which have already accumulated the majority of their final stellar mass but are still accreting matter from a residual envelope plus accretion disk (Lada 1987; M 87; André & Montmerle 1994 – hereafter AM94; Chen et al. 1995). Class II and Class III YSOs, with falling infrared SEDs, correspond to pre-main sequence (PMS) stars, e.g., T Tauri stars (see Bertout 1989 for a review), surrounded by a circumstellar disk (optically thick and optically thin, respectively). For the practical purposes of this paper, we have assigned an SED class to each source of Table 2 based on the following limiting ranges of bolometric temperature (cf. Chen et al. 1995, 1997; Gregersen et al. 1997): $T_{\rm bol} < 70$ K for Class 0, 70 K $\leq T_{\rm bol} <$ 650 K for Class I, and 650 K $\leq T_{\rm bol} <$ 2 880 K for Class II. Note that most of the IRAS Bok globules and Perseus YSOs observed here are confirmed Class 0 protostars (cf. Table 1 of AWB2000).

### 2.2. Bolometer mapping

We carried out our 1.3 mm mapping survey during five observing sessions from 1993 to 1999. All the runs were performed using the IRAM 30 m telescope on Pico Veleta (Spain) and the MPIfR bolometer arrays (now called MAMBO, e.g. Kreysa et al. 1998) with 7 channels (in 1993 and 1994), 19 channels (in 1995 and 1996), and 37 channels (in 1999). The passband of these bolometers has an equivalent width $\approx$70 GHz and is centered at $\nu_{\rm eff} \approx 240$ GHz (e.g. Kreysa et al. 1998).

Each YSO of Table 1 was first observed at its nominal infrared position in the "on-off" observing mode, and then mapped in the "multi-point" or "on-the-fly" mode.

The multi-point mapping mode was mainly used in 1993, for sources which were too weak to be observed in the on-the-fly mapping mode with the 7-channel bolometer. Each multi-point map consists of several ($> 5$) on-off integrations giving fluxes at a few ($> 5 \times 7 = 35$) offsets around the nominal source position.

In the dual-beam on-the-fly mapping mode, the telescope is scanned continuously in azimuth along each row while wobbling. For each channel, the raw data corresponding to a single on-the-fly coverage consist of several rows taken at a series of elevations. We used a scanning velocity of 4″/s or 8″/s, and a sampling of 2″ (resp. 4″) in azimuth and 4″ in elevation. The wobbler frequency was set to 2 Hz and the wobbler throw (in azimuth) was typically 32″. The typical size of the maps depends on the bolometer array used: $\sim 1' \times 1'$, $\sim 3' \times 2'$, and $\sim 4' \times 3'$ for the 7-channel, 19-channel, and 37-channel arrays, respectively.

The dual-beam maps were reduced with the IRAM software for bolometer-array data ("NIC"; cf. Broguière et al. 1995) which uses the EKH restoration algorithm (Emerson et al. 1979).

The *FWHM* size of the main beam was measured to be $HPBW \sim 11''-12''$ using Uranus, Mars, and other strong point-like sources such as quasars[2]. The absolute pointing

[2] The effective resolution of the telescope improved slightly from 1993 to 1995 due to holographic adjustments of the dish panels.

**Table 1.** Sample of observed embedded YSOs

| IRAS and other source names | Adopted name [1] | Coordinates $\alpha_{1950}$ | Coordinates $\delta_{1950}$ | $d$ (pc) | $T_{\rm bol}$ (K) | $L_{\rm bol}$ ($L_\odot$) | Coord. ref. [2] | Lum. ref. [3] |
|---|---|---|---|---|---|---|---|---|
| M04016+2610 | L1489 | $04^{\rm h}01^{\rm m}40\overset{\rm s}{.}6$ | $26°10'49''$ | 140 | 238 | 3.7 | 21 | 22 |
| M04108+2803A | M04108-A | $04^{\rm h}10^{\rm m}47\overset{\rm s}{.}3$ | $28°03'49''$ | 140 | | 0.1 | 21 | 17 |
| M04108+2803B | M04108-B | $04^{\rm h}10^{\rm m}49\overset{\rm s}{.}3$ | $28°03'57''$ | 140 | 205 | 0.6 | 21 | 17 |
| K04113+2758 | K04113 | $04^{\rm h}11^{\rm m}20\overset{\rm s}{.}8$ | $27°58'33''$ | 140 | 606 | $> 1.6$ | 27 | 17 |
| H04145+2812/V892 Tau | Elias1 | $04^{\rm h}15^{\rm m}34\overset{\rm s}{.}5$ | $28°12'02''$ | 140 | 3 226 | 16 | 7 | 7 |
| K04158+2805 | K04158 | $04^{\rm h}15^{\rm m}52\overset{\rm s}{.}2$ | $28°05'10''$ | 140 | 528 | $> 0.4$ | 15 | 17 |
| K04166+2706 | K04166 | $04^{\rm h}16^{\rm m}37\overset{\rm s}{.}8$ | $27°06'29''$ | 140 | 139 | 0.3 | 15 | 17 |
| K04169+2702 | K04169 | $04^{\rm h}16^{\rm m}53\overset{\rm s}{.}8$ | $27°02'48''$ | 140 | 170 | 0.8 | 15 | 17 |
| K04181+2655 | K04181+2655 | $04^{\rm h}18^{\rm m}06\overset{\rm s}{.}4$ | $26°55'01''$ | 140 | 278 | 0.4 | 15 | 17 |
| K04181+2654 | K04181+2654 | $04^{\rm h}18^{\rm m}06\overset{\rm s}{.}9$ | $26°54'04''$ | 140 | 346 | 0.5 | 15 | 17 |
| IRAM04191+1523 | IRAM 04191 | $04^{\rm h}19^{\rm m}06\overset{\rm s}{.}4$ | $15°22'46''$ | 140 | 18 | 0.15 | 1 | 1 |
| T04191+1523 | T04191 | $04^{\rm h}19^{\rm m}09\overset{\rm s}{.}6$ | $15°23'20''$ | 140 | 210 | 0.5 | 27 | 22 |
| M04239+2436 | M04239 | $04^{\rm h}23^{\rm m}54\overset{\rm s}{.}5$ | $24°36'54''$ | 140 | 236 | 1.3 | 21 | 17 |
| M04248+2612/HH31IRS2 | M04248 | $04^{\rm h}24^{\rm m}52\overset{\rm s}{.}7$ | $26°12'42''$ | 140 | 334 | 0.4 | 21 | 17 |
| Z04260+2642 | Z04260 | $04^{\rm h}26^{\rm m}00\overset{\rm s}{.}0$ | $26°42'32''$ | 140 | | 0.1 | 9 | 17 |
| 04263+2426/GVTauB | Haro6-10 | $04^{\rm h}26^{\rm m}22\overset{\rm s}{.}0$ | $24°26'30''$ | 140 | 253 | 7.0 | 21 | 17 |
| K04264+2433 | Elias6 | $04^{\rm h}26^{\rm m}28\overset{\rm s}{.}1$ | $24°33'24''$ | 140 | 252 | 0.5 | 15 | 9 |
| F04287+1801 | L1551-IRS5 | $04^{\rm h}28^{\rm m}40\overset{\rm s}{.}2$ | $18°01'42''$ | 140 | 97 | 28 | 14 | 10 |
| 04287+1806 | HH30-IRS | $04^{\rm h}28^{\rm m}43\overset{\rm s}{.}3$ | $18°06'02''$ | 140 | | $> 0.1$ | 20 | 24 |
| 04287+1807/Haro6-14 | HLTau | $04^{\rm h}28^{\rm m}44\overset{\rm s}{.}4$ | $18°07'36''$ | 140 | 576 | 7.1 | 7 | 24 |
| 04288+1802 | L1551-NE | $04^{\rm h}28^{\rm m}50\overset{\rm s}{.}4$ | $18°02'10''$ | 140 | 75 | 6 | 21 | 5 |
| M04295+2251/L1536-IRS | M04295 | $04^{\rm h}29^{\rm m}32\overset{\rm s}{.}2$ | $22°51'11''$ | 140 | 447 | 0.6 | 21 | 21 |
| 04296+1725 | GGTau | $04^{\rm h}29^{\rm m}37\overset{\rm s}{.}2$ | $17°25'22''$ | 140 | 2 621 | 2.0 | 7 | 17 |
| K04302+2247 | K04302 | $04^{\rm h}30^{\rm m}16\overset{\rm s}{.}8$ | $22°47'04''$ | 140 | 202 | 0.3 | 16 | 17 |
| T04325+2402/L1535-IRS | T04325 | $04^{\rm h}32^{\rm m}33\overset{\rm s}{.}5$ | $24°02'15''$ | 140 | 157 | 0.9 | 27 | 22 |
| K04361+2547 | TMR1 | $04^{\rm h}36^{\rm m}09\overset{\rm s}{.}8$ | $25°47'28''$ | 140 | 144 | 3.7 | 16 | 22 |
| M04365+2535/L1534 | TMC1A | $04^{\rm h}36^{\rm m}31\overset{\rm s}{.}2$ | $25°35'56''$ | 140 | 172 | 2.4 | 21 | 21 |
| K04368+2557 | L1527 | $04^{\rm h}36^{\rm m}49\overset{\rm s}{.}5$ | $25°57'16''$ | 140 | 59 | 1.6 | 18 | 15 |
| M04381+2540/TMC1 | M04381 | $04^{\rm h}38^{\rm m}08\overset{\rm s}{.}5$ | $25°40'53''$ | 140 | 139 | 0.7 | 21 | 21 |
| M04385+2550/Haro6-33 | TMC1C | $04^{\rm h}38^{\rm m}34\overset{\rm s}{.}6$ | $25°50'44''$ | 140 | 636 | $> 0.4$ | 21 | 17 |
| M04489+3042 | M04489 | $04^{\rm h}48^{\rm m}55\overset{\rm s}{.}2$ | $30°42'18''$ | 140 | 399 | 0.3 | 21 | 21 |
| 05417+0907 | B35 | $05^{\rm h}41^{\rm m}44\overset{\rm s}{.}8$ | $09°07'38''$ | 460 | | 15 | 28 | 8 |
| 16442-0930 | L260 | $16^{\rm h}44^{\rm m}13\overset{\rm s}{.}9$ | $-09°29'59''$ | 160 | | 1.0 | 21 | 21 |
| 18148-0440 | L483-MM | $18^{\rm h}14^{\rm m}50\overset{\rm s}{.}6$ | $-04°40'49''$ | 200 | 48 | 14 | 23 | 18 |
| 18331-0035 | L588 | $18^{\rm h}33^{\rm m}07\overset{\rm s}{.}6$ | $-00°35'48''$ | 200 | | ? | 23 | |
| 19156+1906 | L723-MM | $19^{\rm h}15^{\rm m}42\overset{\rm s}{.}0$ | $19°06'55''$ | 300 | 39 | 3 | 2 | 12 |
| 19345+0727 | B335 | $19^{\rm h}34^{\rm m}35\overset{\rm s}{.}1$ | $07°27'24''$ | 250 | 29 | 3 | 3 | 12 |
| 20386+6751 | L1157-MM | $20^{\rm h}38^{\rm m}39\overset{\rm s}{.}6$ | $67°51'33''$ | 440 | 42 | 11 | 30 | 30 |
| 21106+4712 | B361 | $21^{\rm h}10^{\rm m}40\overset{\rm s}{.}9$ | $47°12'01''$ | 350 | | 4.7 | 8 | 8 |
| 23238+7401 | L1262 | $23^{\rm h}23^{\rm m}48\overset{\rm s}{.}7$ | $74°01'08''$ | 200 | | 2.3 | 8 | 29 |
| | L1448-NW | $03^{\rm h}22^{\rm m}31\overset{\rm s}{.}1$ | $30°35'04''$ | 300 | 24 | 2.7 | 6 | 6 |
| 03225+3034/L1448-IRS3 | L1448-N | $03^{\rm h}22^{\rm m}31\overset{\rm s}{.}8$ | $30°34'45''$ | 300 | 55 | 11 | 11 | 6 |
| L1448-MM | L1448-C | $03^{\rm h}22^{\rm m}34\overset{\rm s}{.}3$ | $30°33'35''$ | 300 | 55 | 8 | 11 | 6 |
| 03258+3104/SVS19 | NGC 1333-IRAS 2 | $03^{\rm h}25^{\rm m}49\overset{\rm s}{.}9$ | $31°04'16''$ | 350 | 41 | 40 | 26 | 13 |
| | NGC 1333-IRAS 4A | $03^{\rm h}26^{\rm m}04\overset{\rm s}{.}8$ | $31°03'14''$ | 350 | 34 | 14 | 25 | 25 |
| | NGC 1333-IRAS 4B | $03^{\rm h}26^{\rm m}06\overset{\rm s}{.}5$ | $31°02'51''$ | 350 | 36 | 14 | 25 | 25 |
| 03282+3035 | IRAS 03282 | $03^{\rm h}28^{\rm m}15\overset{\rm s}{.}8$ | $30°35'20''$ | 300 | 23 | 1.5 | 4 | 6 |
| | HH211-MM | $03^{\rm h}40^{\rm m}48\overset{\rm s}{.}7$ | $31°51'24''$ | 300 | | $< 10$? | 19 | |
| M03445+3242/B5-B | B5-IRS1 | $03^{\rm h}44^{\rm m}31\overset{\rm s}{.}8$ | $32°42'34''$ | 300 | | 9.4 | 21 | 21 |

Notes: [1] The first letter of the adopted name generally refers to source samples. Thus, "L" corresponds to the Lynds catalogue (1962); "M" and "K" recall IRAS sources selected by M 87 and Kenyon et al. (1990, 1993a, 1993); "H" and "T" indicate sources studied by Heyer et al. (1987) and Tamura et al. (1991); "Z" and "F" refer to Beichman et al. (1986).
[2] and [3] References: (1) AMB99; (2) and (3) Anglada et al. (1991, 1992); (4) Bachiller et al. (1994); (5) and (6) Barsony et al. (1993, 1998); (7) Beckwith et al. (1990); (8) and (9) Beichman et al. (1986, 1992); (10) Butner et al. (1991); (11) Curiel et al. (1990); (12) Davidson (1987); (13) Jennings et al. (1987); (14) Keene & Masson (1990); (15) KHSS90; (16) KCH93; (17) Kenyon & Hartmann (1993); (18) Ladd et al. (1991); (19) McCaughrean et al. (1994); (20) Mundt et al. (1987); (21) M 87; (22) Ohashi et al. (1996); (23) Parker (1988); (24) Reipurth et al. (1993); (25) and (26) Sandell et al. (1991, 1994); (27) Tamura et al. (1991); (28) and (29) Terebey et al. (1992, 1993); (30) Umemoto et al. (1992).

of the telescope was checked every ∼1 hr and found to be accurate to better than ∼3″–5″ (maximum deviation in both coordinates).

Most of the data benefited from good weather conditions. The zenith atmospheric optical depth, monitored by "skydips" every 1–2 hr, was between ∼0.1 and ∼0.4. Calibration was achieved through on-the-fly mapping and on-off observations of the primary calibrators Uranus and Mars (e.g. Griffin & Orton 1993 and references therein). In addition, L1551-IRS5 and L1448-N were used as secondary calibrators in Taurus and Perseus, respectively. The 1.3 mm flux densities adopted for L1551-IRS5 are ∼1.5 Jy in an 11″ beam and ∼3.4 Jy integrated over a 60″ diameter aperture. L1551-IRS5 was mapped once a day and observed in the on-off mode before and after each YSO map in Taurus. Likewise, L1448-N whose adopted 1.3 mm peak flux is ∼4.1 Jy/beam was observed before and after each map in Perseus. The relative calibration accuracy was found to be better than ∼10% in Taurus by comparing independent observations of sources mapped several times. Within the subsample of isolated IRAS globules and Perseus protostars, the relative calibration accuracy is slightly worse, i.e., ∼20%. The overall, absolute calibration uncertainty is estimated to be ∼20%.

## 3. Results: 1.3 mm continuum images and circumstellar masses

Our on-the-fly 1.3 mm continuum maps are presented in Figs. 1 and 9 (for Taurus sources), in Figs. 2a–c and 10a–d (for isolated globules), and in Figs. 2d,e and 10e–g (for YSOs in Perseus). (Figs. 9 and 10 are only available in electronic form at `http://www.edpsciences.org`.)

It is apparent from the maps that most sources are associated with spatially resolved 1.3 mm dust emission, as expected for "bona fide" embedded protostars surrounded by extended, relatively massive circumstellar envelopes. Surprisingly enough, however, 10 of the 27 candidate protostars of our Taurus subsample are barely resolved and one (K04181+2655) is even not detected. In the following, these 11 Taurus embedded YSOs, as well as the isolated IRAS globule L260 (with similar 1.3 mm properties), will be called "peculiar Class I sources"[3].

The maps also demonstrate that none of the objects of our sample is truly isolated. Most, if not all, of them must have formed in groups (especially in Perseus). At least seven of our maps show evidence for diffuse cloud emission and reveal the presence of new starless dense cores/fragments in the vicinity of the targeted YSOs of Table 1 (see Col. 8 of Table 2).

Basic information extracted from these maps is provided in Table 2 for the YSO sources of Table 1, and in Table 3 for the dense cores without IRAS emission. Table 2 lists the adopted name (Col. 1), the SED class (Col. 2, determined from the $T_{\rm bol}$ value of Table 1), the observing mode and year of observation (Col. 3), the peak and integrated flux densities (Cols. 4 and 5), the estimated circumstellar mass within a radius of 4 200 AU (Col. 6), the degree of flux concentration ($S^{11''}/S^{60''}$ in Col. 7), and a short description of the source environment (Col. 8). Table 3 gives similar information for the new starless cores.

[3] Although NGC 1333-IRAS 4B is similarly unresolved by our 30 m observations, there is independent evidence pointing to the presence of a compact, massive envelope in this more distant (Perseus) Class 0 object (see, e.g. Sect. 3.2).

### 3.1. Circumstellar mass estimates

Since dust continuum emission is largely optically thin at 1.3 mm, our bolometer maps should primarily reflect the dust column density distribution within the observed circumstellar envelopes. If the dust properties and the gas-to-dust ratio are uniform, the 1.3 mm flux density $S_{1.3\ \rm mm}^{\rm beam}$ measured in a single beam should even be directly proportional to the total (gas + dust) beam-averaged column density along the line of sight: $S_{1.3\ \rm mm}^{\rm beam} \propto \kappa_{1.3\ \rm mm}\ B_{1.3\ \rm mm}(T_{\rm dust}) \times < N_{\rm H2} >_{\rm beam}$, where $\kappa_{1.3\ \rm mm}$ is the dust opacity per unit mass column density at $\lambda = 1.3$ mm, and $B_{1.3\ \rm mm}(T_{\rm dust})$ is the Planck function for a dust temperature $T_{\rm dust}$ (see, e.g., MAN98 for a complete equation). Accordingly, the integrated flux density is directly related to the total mass of emitting material. Column 6 of Table 2 gives the circumstellar mass contained within a radius of 4 200 AU of each object, derived from the 1.3 mm flux density integrated over a $30'' \times (d/140\ {\rm pc})^{-1}$ radius circle, $S_{1.3\ \rm mm}^{\rm int}$ (listed in Col. 5), as follows:

$$M_{\rm c\star}^{4200\ \rm AU} = \frac{S_{1.3\ \rm mm}^{\rm int}\ d^2}{\kappa_{1.3\ \rm mm}\ B_{1.3\ \rm mm}(T_{\rm dust})} \simeq 5.3\ 10^{-3}\ M_\odot \times \left(\frac{S_{1.3\ \rm mm}^{\rm int}}{10\ {\rm mJy}}\right) \left(\frac{d}{140\ {\rm pc}}\right)^2 \times \left(\frac{\kappa_{1.3\ \rm mm}}{0.01\ {\rm cm^2\ g^{-1}}}\right)^{-1} \left(\frac{< T_{\rm dust} >}{15\ {\rm K}}\right)^{-1}. \quad (1)$$

For consistency with previous work (e.g. AM94, AWM96, MAN98), we adopted dust opacities per unit (gas + dust) mass column density of $\kappa_{1.3\ \rm mm} = 0.005\ {\rm cm^2\,g^{-1}}$, $\kappa_{1.3\ \rm mm} = 0.01\ {\rm cm^2\,g^{-1}}$, and $\kappa_{1.3\ \rm mm} = 0.02\ {\rm cm^2\,g^{-1}}$ for starless cores, envelopes of Class 0/Class I protostars, and disks around Class II sources, respectively. These opacities correspond to the values recommended by Henning et al. (1995) assuming a gas-to-dust mass ratio of 100. Considering the likely evolution of the gas-to-dust mass ratio (cf. Ciolek & Mouschovias 1996) and of the dust properties themselves (Henning et al. 1995), the adopted opacities are believed to be uncertain by a factor of $\gtrsim 2$ on either side of the quoted values. This is in agreement with models of dust in protostellar cores (e.g. Ossenkopf & Henning 1994), laboratory measurements (Agladze et al. 1996), and recent cross-comparisons with dust *extinction* observations (Kramer et al. 1999).

The value $< T_{\rm dust} >$ used for the dust temperature in Eq. (1) corresponds to a mass-weighted average calculated up to a radius of 4 200 AU (i.e., an angular

**Table 2.** Circumstellar fluxes and masses

| Adopted source name | SED class | Observing method [1] | $S_{1.3\ \mathrm{mm}}^{\mathrm{peak}}$ [2] (mJy/beam) | $S_{1.3\ \mathrm{mm}}^{\mathrm{int}}$ [3] (mJy) | $M_{\mathrm{c}\star}^{4200\ \mathrm{AU}}$ [4] ($M_\odot$) | Concentration $S^{11''}/S^{60''}$ [5] | Source environment |
|---|---|---|---|---|---|---|---|
| L1489 | I | 6×otf9699 | $130 \pm 5$ | 150 | 0.03 | U, 90% | L1489-NH3 |
| M04108-A | II | 2×otf99 | $< 20$ | - | $< 0.002$ | - | L1495N-NH3 |
| M04108-B | I | 2×otf99 | $39 \pm 5$ | 39 | 0.008 | U, 100% | L1495N-NH3 |
| K04113 | I | otf99 | $410 \pm 40$ | 750 | 0.4 | 55% | diffuse cloud |
| Elias1 | II | otf94 | $270 \pm 35$ | 270 | 0.03 | U, 100% | |
| K04158 | I | otf96 | $110 \pm 5$ | 110 | 0.025 | U, 100% | |
| K04166 | 0/I | 2×otf9599 | $180 \pm 8$ | 800 | 0.45 | 20% | |
| K04169 | I | 2×otf9599 | $190 \pm 9$ | 730 | 0.40 | 30% | K04169-NW |
| K04181+2655 | I | 2×otf9699 | $< 10$ | - | $< 0.002$ | - | K04181+2654 |
| K04181+2654 | I | 2×otf9699 | $50 \pm 8$ | 230 | 0.12 | 20% | |
| IRAM04191 | 0 | 3×otf9599 | $110 \pm 7$ | 650 | $0.45^{12.5\mathrm{K}}$ | 20% | T04191 |
| T04191 | I | 3×otf9599 | $110 \pm 7$ | 400 | 0.2 | 30% | IRAM04191 |
| M04239 | I | mpt93 | $80 \pm 10$ | 170 | $\sim$0.09 | $\sim$ 50% | |
| M04248 | I | 2×otf99 | $60 \pm 7$ | 450 | 0.25 | 10% | B217-NH3 |
| Z04260 | I | 2×otf99 | $105 \pm 10$ | 120 | 0.025 | U, 90% | |
| Haro6-10 | I | 2×mpt93 | $100 \pm 10$ | 200 | $\sim 0.07^{20\mathrm{K}}$ | $\sim$50% | |
| Elias6 | I | otf99 | $31 \pm 8$ | 31 | 0.007 | U, 100% | |
| L1551-IRS5 | I | 4×otf99 | $1\,500 \pm 7$ | 3 400 | $0.90^{25\mathrm{K}}$ | 40% | L1551-NE |
| HH30-IRS | I/II | otf99 | $35 \pm 10$ | 35 | 0.008 | U, 100% | HLTau, diffuse cloud |
| HLTau | II | otf99 | $960 \pm 10$ | 1 200 | 0.13 | U, 80% | diffuse cloud |
| L1551-NE | I | 2×otf99 | $850 \pm 10$ | 1 500 | $0.55^{20\mathrm{K}}$ | 60% | IRS5, cloud fragments |
| M04295 | I | otf96 | $115 \pm 10$ | 115 | 0.025 | U, 100% | |
| GGTau | II | otf93 | $665 \pm 10$ | 665 | 0.07 | U, 100% | |
| K04302 | I | otf96 | $180 \pm 10$ | 180 | 0.04 | U, 100% | |
| T04325 | I | 3×otf99 | $110 \pm 7$ | 520 | 0.3 | 20% | L1535-NW, cl. fragment |
| TMR1 | I | otf99 | $110 \pm 8$ | 440 | 0.25 | 25% | diffuse cloud |
| TMC1A | I | mpt93 | $230 \pm 10$ | 450 | $\sim$0.25 | $\sim$50% | |
| L1527 | 0 | 2×otf95 | $375 \pm 6$ | 1 500 | 0.80 | 25% | cloud fragment |
| M04381 | I | otf99 | $70 \pm 9$ | 300 | 0.16 | 20% | diffuse cloud |
| TMC1C | I | otf99 | $30 \pm 5$ | 30 | 0.007 | U, 100% | |
| M04489 | I | otf99 | $15 \pm 4$ | $\gtrsim 15$ | $\gtrsim 0.003$ | U, 100% | |
| B35 | I | mpt93 | $210 \pm 5$ | 820 | $\sim$4.0 | $\sim$30% | |
| L260 | I | otf94 | $110 \pm 5$ | 110 | 0.03 | U, 100% | diffuse cloud L260-NH3 |
| L483-MM | 0 | otf93 | $290 \pm 15$ | 1 100 | 0.8 | 15% | |
| L588 | I | otf93 | $295 \pm 5$ | 570 | 0.4 | 40% | |
| L723-MM | 0 | otf94 | $270 \pm 20$ | 370 | 0.6 | 40% | |
| B335 | 0 | 3×otf9495 | $270 \pm 5$ | 780 | 0.9 | 20% | |
| L1157-MM | 0 | otf94 | $630 \pm 10$ | 630 | 2.0 | 40% | |
| B361 | I | otf96 | $170 \pm 10$ | 190 | 0.4 | 50% | B361-NH3 |
| L1262 | I | 2×mpt94 | $120 \pm 15$ | 500 | $\sim$0.35 | $\sim$20% | |
| L1448-NW | 0 | otf93 | $560 \pm 25$ | 900 | 1.5 | 35% | L1448-N and cloud |
| L1448-N | 0 | otf93 | $1\,400 \pm 5$ | 2 100 | 3.5 | 40% | L1448-C, -NW and cloud |
| L1448-C | 0 | otf93 | $620 \pm 15$ | 910 | 1.5 | 40% | L1448-N and cloud |
| NGC 1333-IRAS 2 | 0 | otf94 | $830 \pm 12$ | 875 | $1.2^{30\mathrm{K}}$ | 40% | cloud fragment |
| NGC 1333-IRAS 4A | 0 | otf93 | $4\,100 \pm 20$ | 4 100 | $4.5^{35\mathrm{K}}$ | 65% | IRAS 4B and cloud |
| NGC 1333-IRAS 4B | 0 | otf93 | $1\,470 \pm 40$ | 1 500 | $1.7^{35\mathrm{K}}$ | U, 90% | IRAS 4A |
| IRAS 03282 | 0 | otf95 | $415 \pm 10$ | 590 | $1.4^{15\mathrm{K}}$ | 40% | |
| HH211-MM | 0 | otf95 | $395 \pm 15$ | 900 | 1.5 | 30% | cloud fragment |
| B5-IRS1 | I | mpt93 | $80 \pm 5$ | 200 | $\sim$0.35 | $\sim$40% | |

Notes: (1) Number, method and date of 1.3 mm observations: "otf" = on-the-fly map; "mpt" = multi-point map. (2) Peak flux in a $11''$–$12''$ beam at source peak. Uncertainty corresponds to $1\sigma$ noise level of on-off and map measurements at peak position, upper limits are $3\sigma$. (3) Flux integrated over a 4 200 AU radius circle for on-the-fly maps, Gaussian integrated flux for multi-point maps. (4) Circumstellar mass within a 4 200 AU radius circle: approximate value derived from multi-point maps. Assumptions on dust opacity and dust temperature are given in Sect. 3.1. (5) Ratio of peak flux (in $11''$-beam) to integrated flux in $60''$ diameter circle. "U" indicates unresolved sources.

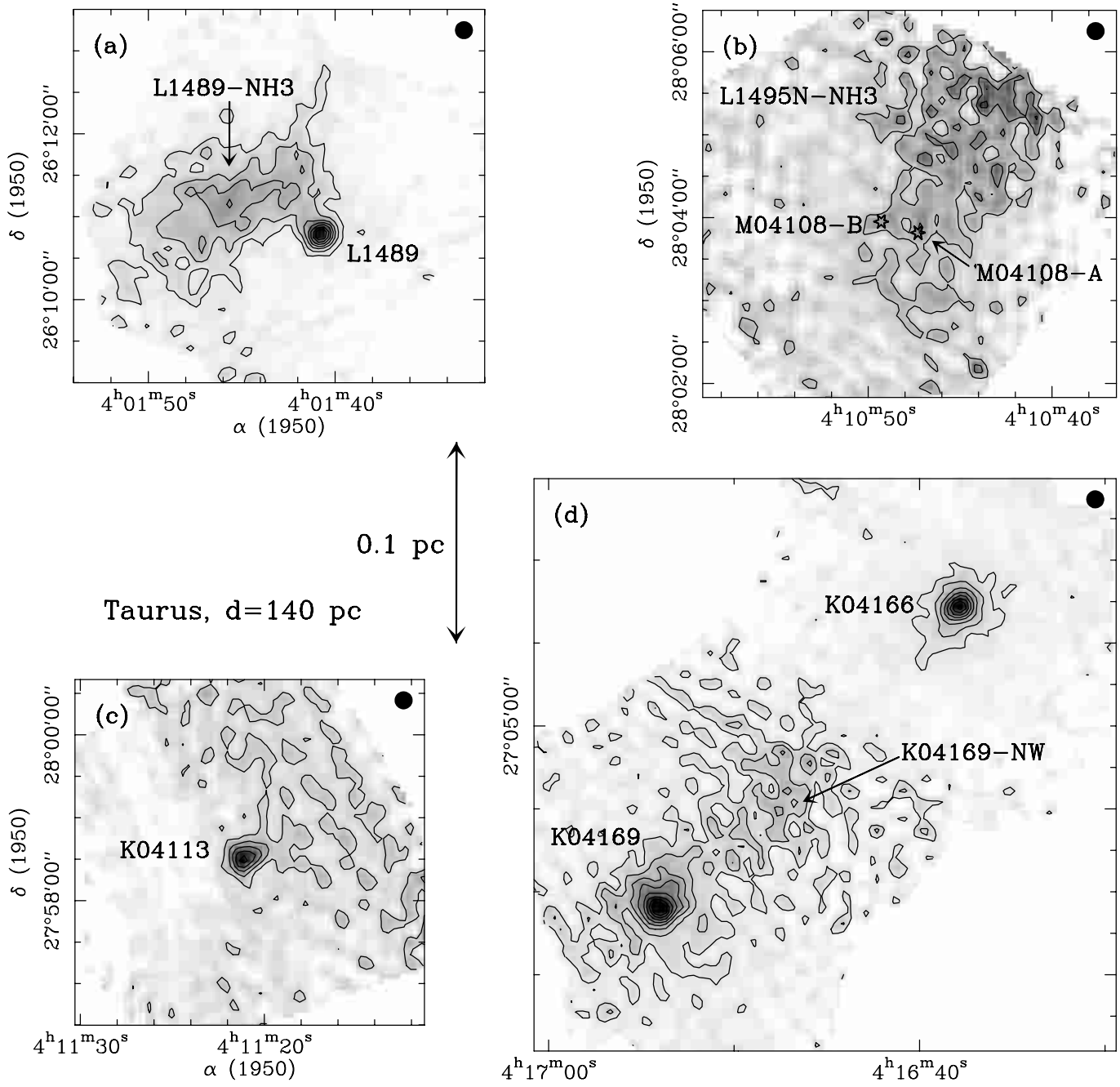


**Fig. 1.** Selection of on-the-fly 1.3 mm continuum maps obtained toward Taurus embedded YSOs (all smoothed to a 13″ effective beam). The positions of YSOs with weak emission and starless fragments are marked by stars and crosses, respectively. Contour levels and rms noise at map center are: **a)** 15 to 120 by 15 mJy/beam, $1\sigma \simeq 4$ mJy/beam; **b)** 35, 70, 105 mJy/beam, $1\sigma \simeq 9.5$ mJy/beam; **c)** 90 to 450 by 90 mJy/beam, $1\sigma \simeq 27$ mJy/beam; **d)** 25 to 200 by 25 mJy/beam, $1\sigma \simeq 6$ to 7 mJy/beam

radius of $30'' \times (d/140\ \mathrm{pc})^{-1}$) and for a centrally-heated sphere with a $\rho(r) \propto r^{-2}$ density gradient ($< T_{\rm dust} >$ would decrease by only 14% if a $\rho(r) \propto r^{-1.5}$ density gradient were adopted instead). In the case of unresolved sources, a similar weighted average temperature was calculated, but only up a radius of 800 AU $\times$ ($d$/140 pc) (i.e. $HPBW/2 \simeq 5.5''$). The radial temperature profile discussed in Sect. 4.3 below was assumed. In practice, this means that we adopted $< T_{\rm dust} >_{4\,200\ \rm AU} = 15$ K for the envelopes surrounding the low-luminosity protostars of Taurus and $< T_{\rm dust} >_{4\,200\ \rm AU} = 20$ K for the more luminous isolated IRAS globules and Perseus protostars. We assumed $< T_{\rm dust } >= 10$ K for the starless cores and $< T_{\rm dust} >_{800\ \rm AU} = 30$ K for the unresolved YSO sources.

The reason why we chose a fiducial radius of 4 200 AU for the circumstellar mass in Eq. (1) and Table 2 is that this roughly corresponds 1) to the head of the expansion wave for a $10^5$-yr old protostar in the inside-out

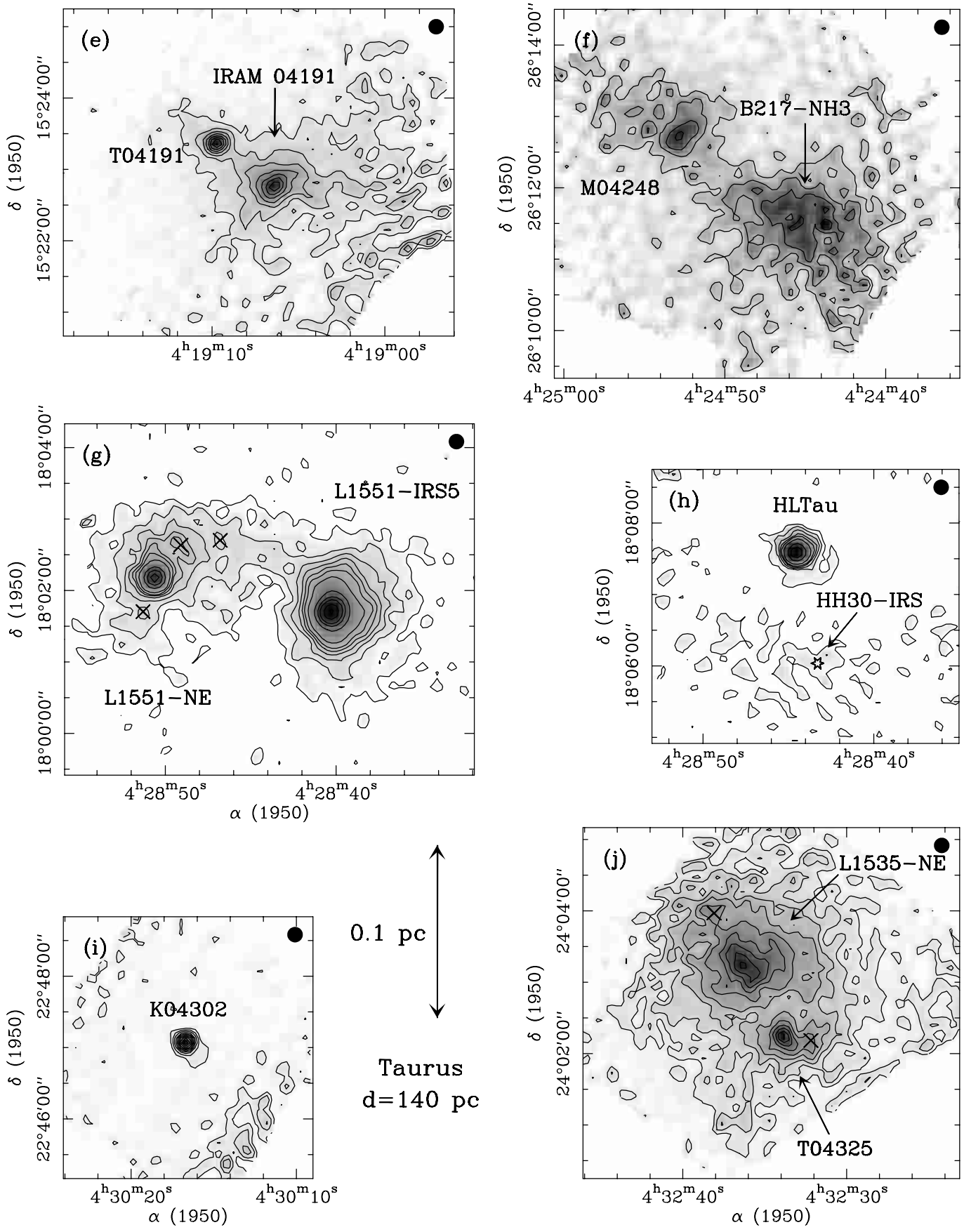


**Fig. 1.** continued. Contour levels and rms noise at map center are: **e)** 17 to 136 by 17 mJy/beam, $1\sigma \simeq 5$ mJy/beam; **f)** 17 to 68 by 17 mJy/beam, $1\sigma \simeq 5$ mJy/beam; **g)** 25 to 150 by 25 mJy/beam, then 200 to 800 by 200 mJy/beam and 1.2, 1.6 Jy/beam, $1\sigma \simeq 6$ to 9 mJy/beam; **h)** 40 to 200 by 40 mJy/beam and then 300, 600, 900 mJy/beam, $1\sigma \simeq 12$ mJy/beam; **i)** 17 to 187 by 17 mJy/beam, $1\sigma \simeq 5$ mJy/beam; **j)** 15 to 135 by 15 mJy/beam, $1\sigma \simeq 4.5$ mJy/beam

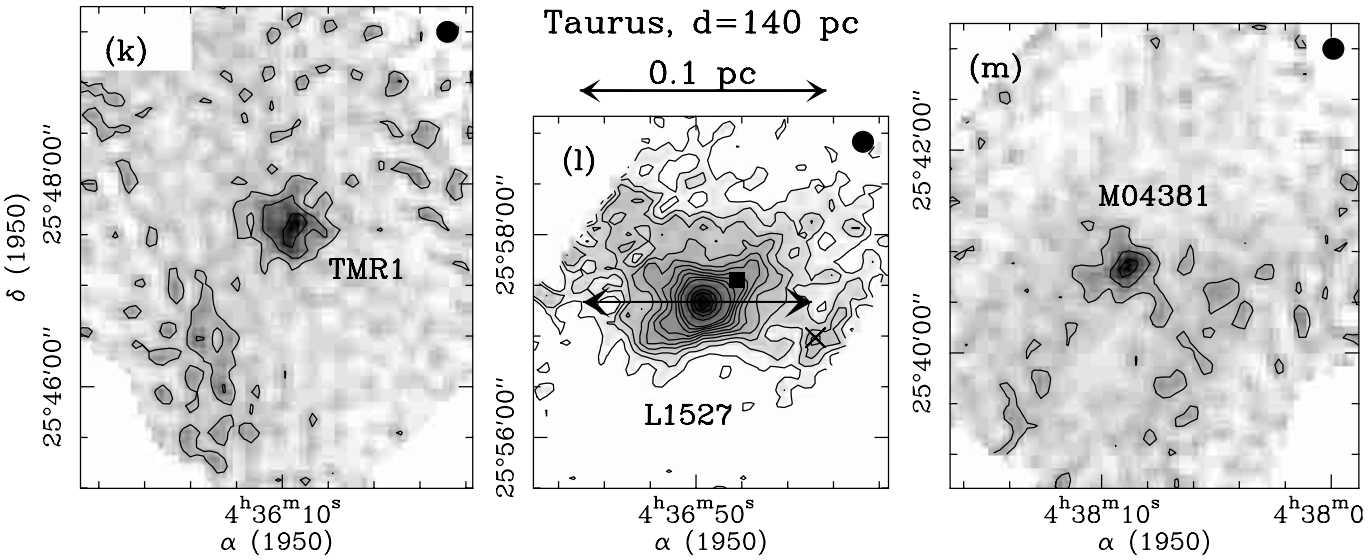


**Fig. 1.** continued. Contour levels and rms noise at map center are: **k)** 40, 80, 120 mJy/beam, $1\sigma \simeq 11$ mJy/beam; **l)** 12 to 120 by 12 mJy/beam and 180 to 420 by 60 mJy/beam, $1\sigma \simeq 3.5$ mJy/beam; **m)** 25, 50, 75 mJy/beam, $1\sigma \simeq 7$ mJy/beam. The outflow axis and proposed companion of L1527 are marked with arrows and a filled square marker in **l)** (cf. MacLeod et al. 1994; Fuller et al. 1996, respectively). See complementary Fig. 9 within the on-line version of this paper

**Table 3.** Cold dense cores with no IRAS emission

| Core name [(1)] | Coordinates $\alpha_{1950}$ | Coordinates $\delta_{1950}$ | $d$ (pc) | $S_{1.3\,\mathrm{mm}}^{\mathrm{peak}}$ [(2)] (mJy/beam) | $S_{1.3\,\mathrm{mm}}^{\mathrm{int}}$ [(3)] (mJy) | $M^{4200\ \mathrm{AU}}$ [(4)] ($M_\odot$) | $R_{\mathrm{out}}$ [(5)] (AU) | $M^{R_{\mathrm{out}}}$ [(6)] ($M_\odot$) |
|---|---|---|---|---|---|---|---|---|
| L1489-NH3 | $04^{\mathrm{h}}01^{\mathrm{m}}45\overset{\mathrm{s}}{.}7$ | $26°11'10''$ | 140 | $55 \pm 5$ | 510 | 1.0 | $15\,000 \pm 3\,000$ | 4. |
| L1495N-NH3 | $04^{\mathrm{h}}10^{\mathrm{m}}45\overset{\mathrm{s}}{.}0$* | $28°05'40''$* | 140 | $(45 \pm 15)$* | ∼500 | ∼1.0 | $\gtrsim 14\,000$ | $> 5.0$* |
| K04169-NW | $04^{\mathrm{h}}16^{\mathrm{m}}47\overset{\mathrm{s}}{.}4$ | $27°04'05''$ | 140 | $50 \pm 15$ | 340 | 0.7 | $\gtrsim 14\,000$ | 2.5 |
| B217-NH3 | $04^{\mathrm{h}}24^{\mathrm{m}}45\overset{\mathrm{s}}{.}8$ | $26°11'30''$ | 140 | $55 \pm 10$ | 560 | 1.1 | $14\,000 \pm 1\,500$ | 5.5 |
| L1535-NE | $04^{\mathrm{h}}32^{\mathrm{m}}36\overset{\mathrm{s}}{.}3$ | $24°03'14''$ | 140 | $100 \pm 7$ | 850 | 1.7 | $\gtrsim 21\,000$ | 7.5 |
| B361-NH3 | $21^{\mathrm{h}}10^{\mathrm{m}}33\overset{\mathrm{s}}{.}7$ | $47°12'46''$ | 350 | $90 \pm 10$ | 130 | 1.6 | $35\,000 \pm 3\,500$ | 25. |

Notes: (1) The "NH3" suffix refers to Benson & Myers (1989); "NE" and "NW" correspond to new dust cores. (2) to (4) Same as in Table 2. (5) Estimated outer radius. (6) Total mass within $R_{\mathrm{out}}$. * The characteristics of L1495N-NH3 are more uncertain as this source was incompletely mapped.

collapse scenario if the sound speed is $a_{\mathrm{s}} \sim 0.2$ km s$^{-1}$ (i.e. $T_{\mathrm{cloud}} \sim 10$ K), and 2) to an angular radius of $30''$ at the distance of Taurus which is comparable to the radius of the IRAS and ISO beams at 60 $\mu$m.

For the entire sample of 27 Taurus candidate protostars (including peculiar Class Is), the median mass enclosed within $r < 4\,200$ AU is $\overline{M_{\mathrm{c}\star}^{4200\ \mathrm{AU}}}(r < 4\,200\ \mathrm{AU}) \sim 0.074\ M_\odot$. This value is not much larger than the typical disk mass found for classical T Tauri stars (Beckwith et al. 1990) or embedded Class II sources (AM94). In contrast, the 16 Taurus sources of Table 2 with spatially resolved emission are bona-fide protostars with significantly more massive circumstellar structures (envelopes/disks): $M_{\mathrm{c}\star}^{4200\ \mathrm{AU}} \sim 0.07 - 0.9\ M_\odot$, corresponding to a median mass $\overline{M_{\mathrm{c}\star}^{4200\ \mathrm{AU}}}(r < 4\,200\ \mathrm{AU}) \sim 0.28\ M_\odot$. The bona-fide protostars observed in Perseus and Bok globules have even larger circumstellar masses: $M_{\mathrm{c}\star}^{4200\ \mathrm{AU}} \sim 0.3{-}5\ M_\odot$ and $M_{\mathrm{c}\star}^{4200\ \mathrm{AU}} \sim 0.3{-}4\ M_\odot$, respectively.

### 3.2. Envelope versus disk mass

A priori, the integrated fluxes listed in Table 2 include contributions from both the protostellar envelope and the circumstellar disk: $S_{1.3\,\mathrm{mm}}^{\mathrm{int}} = S_{1.3\,\mathrm{mm}}^{\mathrm{env}} + S_{1.3\,\mathrm{mm}}^{\mathrm{disk}}$. The disk contribution must be properly assessed if an accurate estimate of the envelope mass is desired.

Predictions made in the framework of the standard theory of isolated protostars suggest that the millimeter continuum flux should be dominated by emission from the envelope rather than from the disk, when observed at the resolution of the IRAM 30 m telescope (e.g. Terebey et al. 1993; Galli 1995). In agreement with these predictions, the median flux concentration $S^{11''}/S^{60''} \sim 30\%$

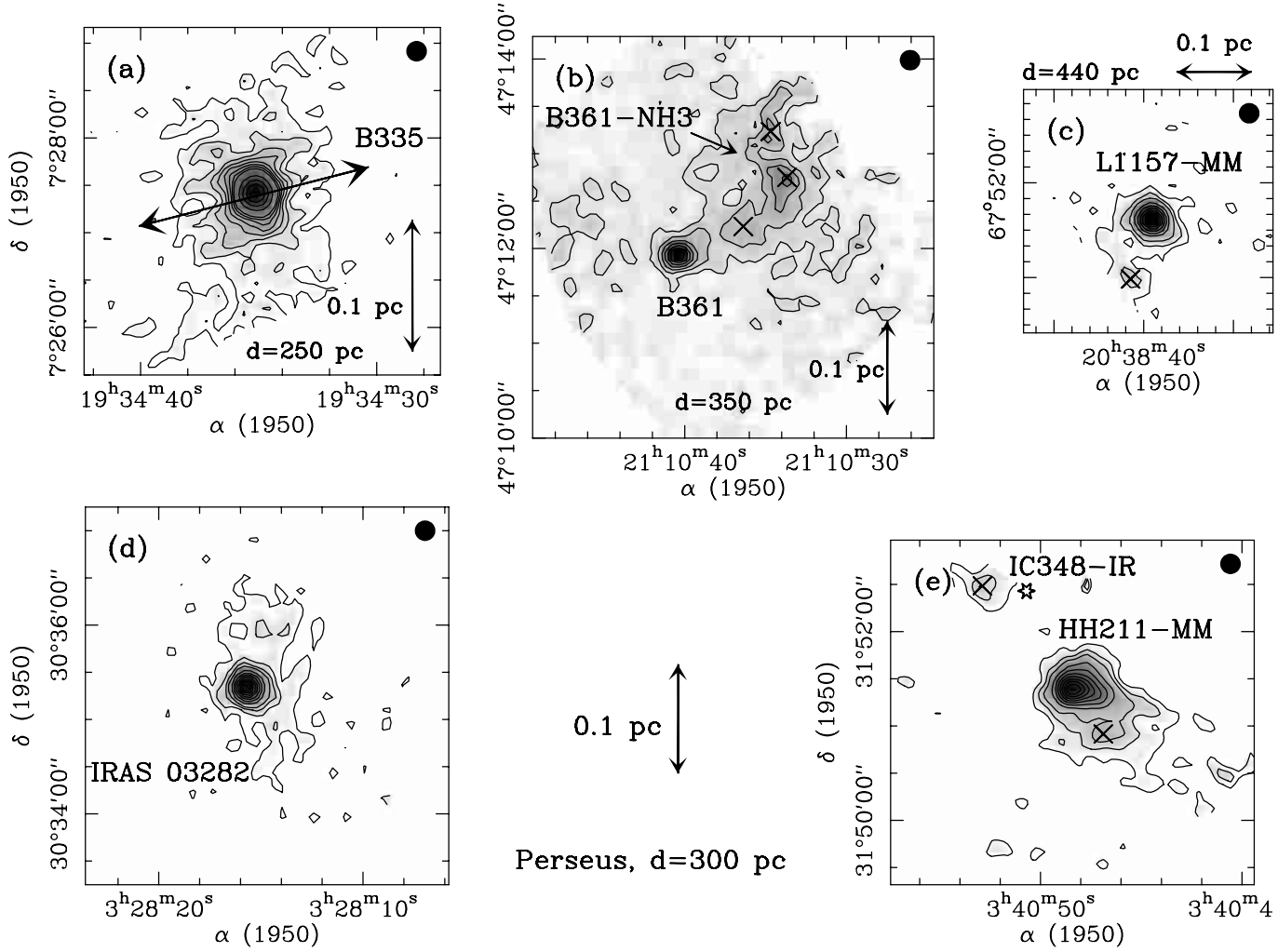


**Fig. 2.** Same as Fig. 1 for several isolated IRAS globules (**a**–**c**) and Perseus protostars (**d**,**e**). Contour levels and rms noise at map center are: **a)** 12 to 96 by 12 mJy/beam and 150 to 300 by 50 mJy/beam, $1\sigma \simeq 3.5$ mJy/beam; **b)** 25 to 175 by 25 mJy/beam, $1\sigma \simeq 7.5$ mJy/beam; **c)** 40 to 120 by 40 mJy/beam and 200 to 600 by 80 mJy/beam, $1\sigma \simeq 11$ mJy/beam; **d)** 25 to 100 by 25 mJy/beam and 150 to 450 by 50 mJy/beam, $1\sigma \simeq 7.5$ mJy/beam; **e)** 30, 60, 90 mJy/beam and 150 to 500 by 50 mJy/beam, $1\sigma \simeq 8.5$ mJy/beam. The axis of the B335 outflow is indicated by arrows in **a)**. See complementary Fig. 10 on-line

estimated for the bona-fide protostars of our sample suggests that $\gtrsim 70\%$ of the *integrated* flux density $S^{\rm int}_{1.3\ {\rm mm}}$ arises from the envelope. Millimeter interferometric observations by, e.g., Hogerheijde et al. (1997) and Motte et al. (2001) provide estimates of the disk component $S^{\rm disk}_{1.3\ {\rm mm}}$ for several bona-fide protostars in Taurus, and confirm that the integrated flux density measured at the 30 m telescope arises primarily from the envelope: $S^{\rm disk}_{1.3\ {\rm mm}}/S^{\rm int}_{1.3\ {\rm mm}}(r < 4\,200\ {\rm AU}) \lesssim 10\%$. A similar conclusion holds in Perseus for the Class 0 protostars NGC 1333-IRAS 4A and NGC 1333-IRAS 4B which, albeit barely resolved at the 11″–13″ resolution of the 30 m and JCMT telescopes (cf. Table 2 and Sandell et al. 1991), are ∼8 times stronger than when observed with the CSO–JCMT interferometer (Lay et al. 1995). More generally, the disk contribution is estimated to be $\lesssim 10\%$ for 8 of the 9 Perseus protostars of our sample (Motte et al. 2001; Looney et al. 2000).

The above discussion suggests that $M_{\rm c\star}^{4200\ {\rm AU}}$ should be a good approximation of the envelope mass within 4 200 AU for all the "self-embedded" sources, even when the exact disk contribution is unknown. In the following, we will thus assume $M_{\rm env}^{4200\ {\rm AU}} \sim M_{\rm c\star}^{4200\ {\rm AU}}$ for all the protostars with spatially resolved envelopes[4] (see Col. 7 of Table 2).

[4] For thirteen objects in our sample, better estimates of $M_{\rm env}^{4200\ {\rm AU}}$ may be derived by subtracting the disk contribution measured at 1.4 mm with interferometers (e.g. Motte et al. 2001). We estimate the true envelope mass to be $M_{\rm env}^{4200\ {\rm AU}} \sim 0.03\ M_\odot$ for L1489, $\sim 0.4\ M_\odot$ for K04166, $\sim 0.35\ M_\odot$for K04169, $\sim 0.45\ M_\odot$ for IRAM 04191, $\sim 0.18\ M_\odot$ for T04191, $\sim 0.75\ M_\odot$ for L1551-IRS5, $\sim 0.2\ M_\odot$ for TMR1, $\sim 0.7\ M_\odot$ for L1527 and $\sim 1.5\ M_\odot$ for L1448-NW, $\sim 2.5\ M_\odot$ for L1448-N, $\sim 1.3\ M_\odot$ for L1448-C, $\sim 1.1\ M_\odot$ for IRAS 03282, $\sim 1.3\ M_\odot$ for HH211-MM.

By contrast, the disk can sometimes contribute a large fraction of the *peak* flux density $S_{1.3\ \mathrm{mm}}^{\mathrm{peak}}$ measured in an $11''$ beam. For the "peculiar", unresolved Class I sources of our sample, most of the circumstellar material may be in a disk, with $S_{1.3\ \mathrm{mm}}^{\mathrm{disk}}/S_{1.3\ \mathrm{mm}}^{\mathrm{peak}} \lesssim 100\%$ (see discussion in Sect. 5.2.3 below). In these cases, the masses listed in Table 2 provide only upper limits to the actual envelope masses: $M_{\mathrm{env}}^{4200\ \mathrm{AU}} < M_{\mathrm{c}\star}^{4200\ \mathrm{AU}}$.

## 4. Radial structure analysis

In this section, we describe our method of deriving the radial density structure of a circumstellar envelope from the observed intensity profile at 1.3 mm, and then apply this method to each source of Table 2.

### 4.1. Radial intensity profiles

The 1.3 mm continuum emission mapped around each YSO is first averaged in circular annuli centered at the peak position. This yields a mean radial intensity profile, $S(\theta)$, where $\theta$ is the angular radius from source center. Depending on the local environment (cf. Col. 8 of Table 2), a fraction of the map has to be masked in order to avoid including emission from neighboring sources such as the fragments apparent in Figs. 1–2. When the map results from the combination of several coverages, we choose the best coverage to derive the intensity profile and make an accurate modeling (see Appendix). The resulting mean radial profiles are shown in Figs. 3a–g and 11a–l for Taurus embedded YSOs, in Figs. 4a–d and 12a–c for isolated globules, and in Figs. 4e–h and 12e–h for Perseus protostars. The radial profiles of several starless cores are also shown in Figs. 3h, 11m–p and 12d. (Figs. 11 and 12 are only available in electronic form at `http://www.edpsciences.org`.)

These radial intensity profiles trace the underlying source column density profiles (see Sect. 3.1 and Eq. (1) of MAN98), although they also depend on the temperature gradient: $S(\theta) \propto N_{\mathrm{H2}}(\theta) \times T(\theta)$ in the Rayleigh-Jeans approximation of the Planck function. Since one expects both $N_{\mathrm{H2}}(\theta)$ and $T(\theta)$ to behave roughly as power-laws over a wide range of angular radii $\theta$ (see Sect. 1 above and Sect. 4.3 below), it is natural to compare the derived radial profiles with those of circularly-symmetric, power-law intensity models of the form $I(\theta) \propto \theta^{-m}$.

As shown by Adams (1991), the same power-law intensity distribution, $\tilde{I}(\theta) \propto \theta^{-m}$, remains *after* convolution with a Gaussian beam, provided that the profile is examined at radii greater than one full beamwidth from the center (i.e., $\theta \geq 11''$ in our case). There is, however, a major complication due to the dual-beam scanning technique, which is addressed by the simulation analysis presented in Appendix. This analysis indicates that a finite-sized, dual-beam scan/map behaves roughly like a high-pass spatial frequency filter suppressing emission on scales larger than the size of the scan/map. In practice, this entails a loss of flux density at large radii in the simulated profiles compared with the intrinsic profiles (see Fig. 7a in Appendix). In order to properly interpret the intensity profile measured toward a given protostellar envelope, we have run an input grid of power-law envelope models through a complete simulation of the mapping and data-reduction processes adapted to this particular source (see, e.g., Fig. 7b in Appendix). We can then estimate the intrinsic power-law index $m$ of the source radial intensity profile (along with its typical uncertainty) by comparison with our output grid of simulated model profiles (cf. Figs. 3–4). The "best-fit" power-law indices $m$ are listed in Col. 3 of Table 4 for all the sources with spatially-resolved envelope emission. These indices apply to the main portion of the observed intensity profile (see the range of angular radii listed in Col. 2 of Table 4). We give an estimate of the envelope outer radius $R_{\mathrm{out}}$ in Col. 7 of Table 4 whenever there is evidence that the power-law regime breaks down in the outer part of the intensity profile.

Most of the sources are spatially extended and have radial intensity profiles that can be fitted reasonably well over the majority of their extent by one of our simulated $I(\theta) \propto \theta^{-m}$ models with $m = 0.4{-}1.8$. Several observed profiles appear to steepen or merge into some cloud emission beyond a finite radius, $R_{\mathrm{out}}$ (see, e.g., Figs. 3f, 4d, and 4g). The presence of background emission from the ambient cloud is sometimes noticeable in the maps themselves (see, e.g., TMR1 in Fig. 1k). The mean column density we estimate for such background emission is $N_{\mathrm{H2}} \sim 2{-}7\ 10^{21}$ cm$^{-2}$ around Taurus protostars and Bok globules (assuming $T_{\mathrm{dust}} = 15$ K and 20 K, respectively), compared to a column density of envelope material ranging from $N_{\mathrm{H2}} \sim 5\ 10^{21}$ cm$^{-2}$ to $N_{\mathrm{H2}} \sim 5\ 10^{23}$ cm$^{-2}$. In Perseus, the background has $N_{\mathrm{H2}} \sim 10^{22}$ cm$^{-2}$, while the envelopes reach $N_{\mathrm{H2}} \sim 10^{24}$ cm$^{-2}$ (if $T_{\mathrm{dust}} = 20$ K).

By contrast, the peculiar Class I sources with compact emission in the maps (cf. Sect. 3) have intensity profiles roughly consistent with the effective point spread function of the 30 m telescope at 1.3 mm (see, e.g., Fig. 3g). This is reminiscent of the radial intensity profiles observed toward Class II sources (cf. AM94).

Finally, we note here that the radial intensity profiles of the cold cores/condensations of Table 3 are flatter than our simulated $I(\theta) \propto \theta^{-m}$ models with $m = 0.5$ in their inner regions (i.e., at $r \lesssim 6\,000$ AU, where we measure $m \lesssim 0.1$ – see the example of L1535-NE in Fig. 3h). This is reminiscent of the pre-stellar cloud cores studied by AWM96 and Ward-Thompson et al. (1999).

### 4.2. Factors influencing the derivation of the envelope radial profile

#### 4.2.1. Disk component

In order to derive the intrinsic profile of the envelope, a central point source corresponding to the possible contribution of a compact, unresolved disk should in principle be subtracted out from the bolometer-array data. However, the disk contribution to the single-dish peak flux density

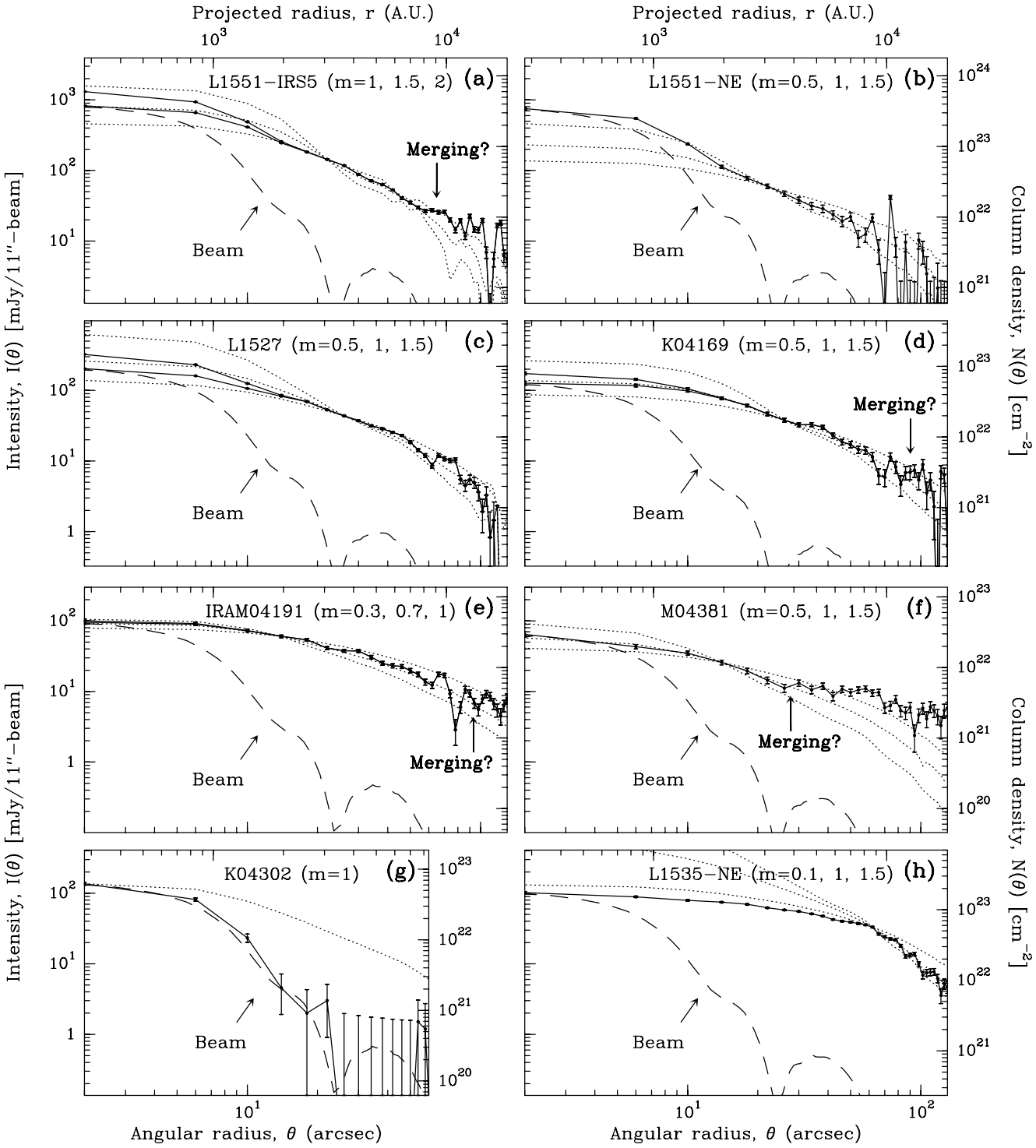


**Fig. 3.** Radial intensity profiles of the environment of 7 embedded YSOs (**a**–**g**) and 1 starless core (**h**). Column density estimates assuming $\kappa_{1.3\ \mathrm{mm}} = 0.01\ \mathrm{cm^2\,g^{-1}}$ and $T_{\mathrm{dust}} = 15$ K are shown on the right axis of each profile (in **h**): $\kappa_{1.3\ \mathrm{mm}} = 0.005\ \mathrm{cm^2\,g^{-1}}$ and $T_{\mathrm{dust}} = 10$ K). The observed profiles (solid curves) are compared with simulated model profiles (dotted curves) and with the 30 m beam (dashed curve). In **a)** and **c**–**e)**, two source profiles are shown, before (upper solid curve) and after (lower solid curve) subtraction of the disk component observed by the IRAM Plateau de Bure interferometer at 1.4 mm (Motte et al. 2001); the latter should correspond to the profile of the envelope *alone*. The input models are all circularly symmetric with infinite power-law profiles, $I(\theta) \propto \theta^{-m}$ (see Appendix). Unlike YSO envelope profiles, the profile of the starless core L1535-NE (in **h**) is not consistent with a single power-law model. See complementary Fig. 11 on-line

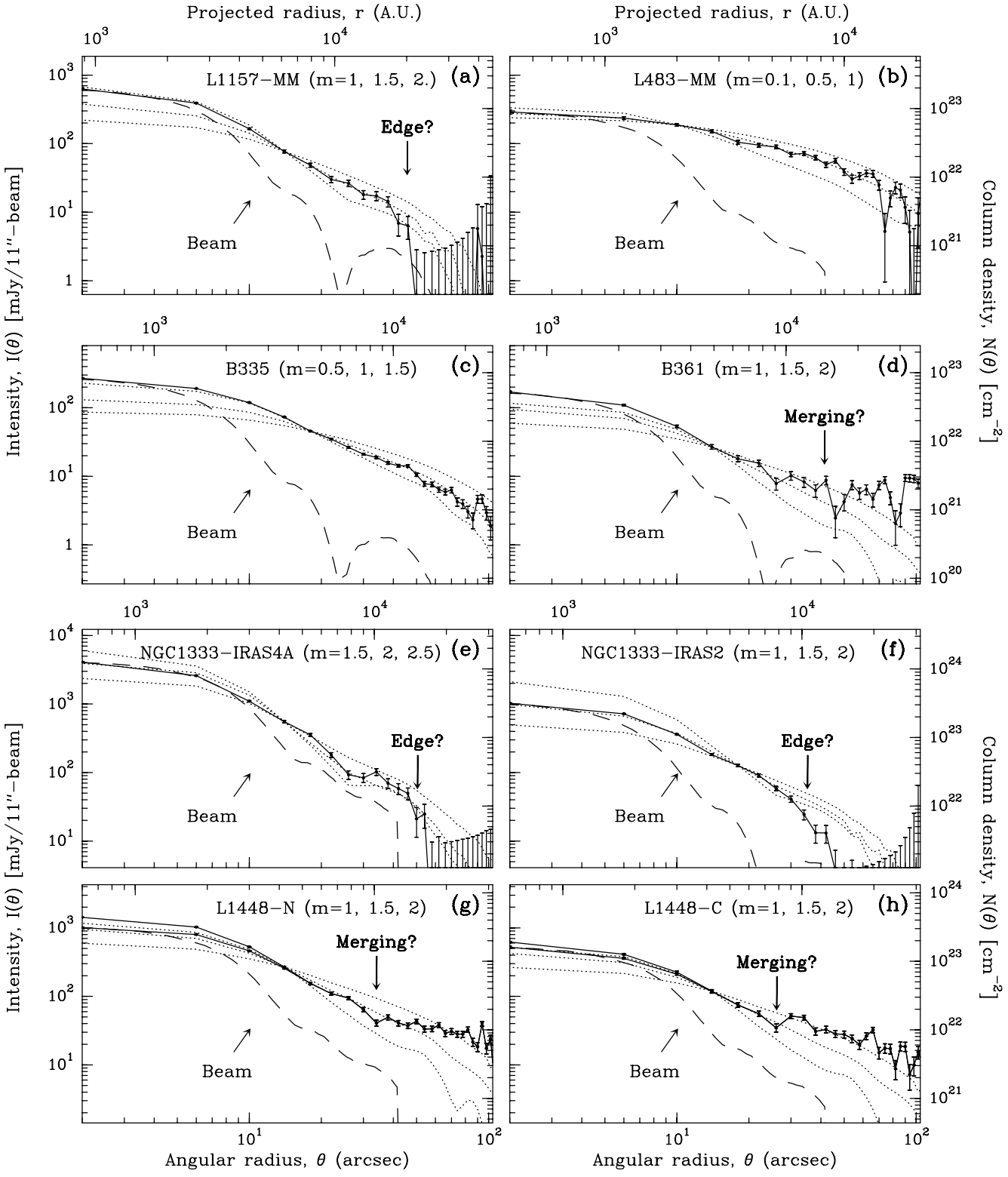


**Fig. 4.** Same as Fig. 3 for 4 isolated globules (**a**–**d**) and 4 Perseus protostars (**e**–**h**). Column density estimates assume $\kappa_{1.3\ \mathrm{mm}} = 0.01\ \mathrm{cm^2\ g^{-1}}$ and $T_{\mathrm{dust}} = 20$ K. In **g,h)**, two source profiles are shown, before (upper solid curve) and after (lower solid curve) subtraction of the disk component observed by the IRAM PdBI interferometer at 1.4 mm (Motte et al. 2001). See complementary Fig. 12 on-line

appears to be small for the bona-fide protostars of our sample. Based on interferometric measurements, Motte et al. (2001) estimate $S_{1.3\ \mathrm{mm}}^{\mathrm{disk}}/S_{1.3\ \mathrm{mm}}^{\mathrm{peak}} \lesssim 30\%$ for 7 Taurus YSOs and 5 Perseus protostars (see also Sect. 3.2). We have simulated the effect of an unresolved disk component of this magnitude and checked that it does *not* affect the

**Table 4.** Results of the radial profile analysis for the spatially resolved envelopes

| Adopted source name | $\theta$ range | $m(\theta)^{(1)}$ | $\theta_{\rm isoth}{}^{(2)}$ ($''$) | $q(\theta)^{(3)}$ | $p$ $= m+1-q$ | $R_{\rm out}$ (AU) | $M_{\rm c\star}^{R_{\rm out}\,(4)}$ ($M_\odot$) | Additional sources of uncertainty |
|---|---|---|---|---|---|---|---|---|
| L1551-IRS5 | $20''$–$65''$ | $1.5\pm0.3$ | $110''$ | 0.4 | $2.1\pm0.4$ | $9\,100\pm700$? | $1.5^{25\rm K}$ | |
| L1551-NE | $11''$–$60''$ | $1\pm0.3$ | $51''$ | 0.4 | $1.6\pm0.4$ | $\gtrsim 8\,500$ | $1.1^{25\rm K}$ | |
| K04113 | $11''$–$55''$ | $1.8\pm1$ | $26''$ | 0.4 | $2.4\pm1$ | $8\,000\pm2\,000$? | 0.4 | |
| L1527 | $11''$–$120''$ | $1\pm0.4^*$ | $26''$ | $\sim$0 | $2.0\pm0.5$ | $\gtrsim 17\,000$ | 1.7 | outflow cavity |
| K04166 | $11''$–$105''$ | $1\pm0.2$ | $11''$ | $-0.2\pm0.2$ | $2.2\pm0.5$ | $\gtrsim 15\,000$ | 1.0 | |
| K04169 | $11''$–$90''$ | $0.8\pm0.2$ | $18''$ | 0 | $1.8\pm0.3$ | $13\,000\pm1\,500$? | 1.1 | |
| T04191 | $11''$–$70''$ | $0.8\pm0.4$ | $15''$ | 0 | $1.8\pm0.5$ | $\gtrsim 10\,000$ | 0.45 | |
| IRAM 04191 | $11''$–$100''$ | $0.6\pm0.1$ | $8''$ | $-0.2\pm0.2$ | $1.8\pm0.4$ | $14\,000\pm1\,500$? | $1.4^{12.5\rm K}$ | |
| T04325 | $11''$–$80''$ | $1.0\pm0.6^*$ | $20''$ | 0 | $2.0\pm0.7$ | $\gtrsim 11\,000$ | 0.7 | within a dense core |
| TMR1 | $11''$–$60''$ | $0.8\pm0.4$ | $40''$ | 0.4 | $1.4\pm0.5$ | $8\,500\pm1\,500$? | 0.4 | |
| M04381 | $11''$–$30''$ | $1.1\pm0.3^*$ | $17''$ | 0 | $2.1\pm0.4$ | $3\,900\pm700$? | 0.16 | within cloud |
| M04248 | $11''$–$80''$ | $0.7\pm0.5^*$ | $13''$ | 0 | $1.7\pm0.6$ | $\gtrsim 11\,000$ | 0.75 | elliptical envelope |
| K04181+2654 | $11''$–$50''$ | $1.2\pm0.6^*$ | $15''$ | 0 | $2.2\pm0.7$ | $\gtrsim 7\,000$ | 0.16 | elliptical envelope |
| L1157-MM | $11''$–$45''$ | $1.5\pm0.2$ | $22''$ | 0 | $2.2\pm0.4^*$ | $20\,000\pm2\,000$? | 6.5 | deprojection |
| L483-MM | $11''$–$90''$ | $0.4\pm0.3^*$ | $54''$ | $0.2\pm0.2$ | $1.2\pm0.6$ | $\gtrsim 18\,000$ | 4. | elliptical envelope |
| L588 | $11''$–$55''$ | $1.5\pm0.5$ | ? | $0.2\pm0.2$ | $2.3\pm0.8$ | $11\,000\pm2\,000$? | 0.8 | |
| B335 | $11''$–$120''$ | $1.2\pm0.3^*$ | $20''$ | 0 | $2.2\pm0.4$ | $\gtrsim 30\,000$ | 2.5 | outflow interaction |
| L723-MM | $11''$–$40''$ | $1.7\pm0.3$ | $17''$ | 0 | $2.5\pm0.5^*$ | $12\,000\pm3\,000$? | 1.2 | deprojection |
| B361 | $11''$–$40''$ | $1.2\pm0.2$ | $18''$ | 0 | $2.0\pm0.4^*$ | $14\,000\pm2\,000$? | 0.9 | deprojection |
| NGC 1333-IRAS4A | $11''$–$50''$ | $1.8\pm0.3$ | $31''$ | $0.2\pm0.2$ | $2.6\pm0.6$ | $17\,000\pm5\,000$? | $8.^{35\rm K}$ | |
| L1448-N | $11''$–$35''$ | $1.7\pm0.2$ | $32''$ | 0.4 | $2.1\pm0.4^*$ | $10\,000\pm1\,500$? | 6 | deprojection |
| L1448-C | $11''$–$25''$ | $1.6\pm0.2$ | $27''$ | 0.4 | $2.0\pm0.4^*$ | $7\,500\pm600$? | 2.5 | deprojection |
| NGC 1333-IRAS2 | $11''$–$35''$ | $1.7\pm0.3$ | $61''$ | 0.4 | $2.0\pm0.5^*$ | $12\,000\pm2\,000$? | $2.5^{30\rm K}$ | deprojection |
| L1448-NW | $11''$–$40''$ | $1.3\pm0.3$ | $16''$ | $0.2\pm0.2$ | $1.8\pm0.7^*$ | $13\,000\pm3\,000$? | 3.5 | deprojection |
| IRAS 03282 | $11''$–$40''$ | $1.6\pm0.4^*$ | $12''$ | 0 | $2.3\pm0.6^*$ | $\gtrsim 12\,000$ | $2.5^{15\rm K}$ | deprojection |
| HH211-MM | $11''$–$45''$ | $1.3\pm0.5^*$ | $<37''$ | $0.2\pm0.2$ | $2.1\pm0.6$ | $\gtrsim 13\,000$ | 2.5 | "cometary" globule |

Notes: (1) Power-law index of the radial intensity profile $S_{1.3\ \rm mm}(\theta)$ over the angular range of Col. 2. (2) Angular radius beyond which heating by the central source is negligible. (3) Power-law index of the radial temperature profile $T(\theta)\propto\theta^{-q}$ over the angular range of Col. 2. (4) Total circumstellar mass within the radius $R_{\rm out}$ of Col. 7 (see Sect. 3.1 for assumed dust opacity and temperature). Star markers in Col. 3 or Col. 6 indicate that additional sources of uncertainty have been taken into account (see Col. 9).

radial intensity profile measured for $\theta > 11''$ (see Fig. 8a in Appendix). We conclude that the disk has a negligible influence on our analysis of the envelope radial profile, even in the case of the Perseus protostars with compact envelopes (cf. Sect. 3.2). To illustrate this point, Figs. 3–4 and Figs. 11–12 show the estimated envelope radial profile before and after subtraction of the disk component when the latter is known.

### 4.2.2. Background cloud

In the presence of filamentary background cloud emission, an intrinsically spherical envelope can artificially look non spherical. The maps of K04169, M04248, and IRAS 03282 (in Figs. 1d, 1f, and 2d) may provide examples of this. In principle, the power-law index $m_{\rm obs}$ of the observed intensity profile should then be corrected by a term $\epsilon_{\rm back}$ to yield the intrinsic index of the source envelope: $m_{\rm env} = m_{\rm obs} + \epsilon_{\rm back}$, where $\epsilon_{\rm back} > 0$ when the effective background emission is positive. (If there is relatively strong background emission just outside the mapped region, part of it may aliased as a *negative* signal in the restored image, in which case $\epsilon_{\rm back} < 0$.) In order to minimize the magnitude of this effect, we measured the intensity profile of each source in the parts of the map least perturbed by any cloud (or companion) emission. For K04169, M04248, and IRAS 03282, we restricted our analysis to sectors perpendicular to the large-scale filamentary emission apparent in Fig. 1d, Fig. 1f, and Fig. 2d. Any remaining background emission should thus be weak compared to the envelope emission itself. We have simulated the

observation of a power-law envelope embedded in a Gaussian background of $FWHM$ size 0.5 pc and peak column density $N_{\rm H2} \sim 10^{21}$–$10^{22}\,{\rm cm}^{-2}$. These simulations suggest that $\epsilon_{\rm back}$ is negligible (i.e., $\epsilon_{\rm back} \lesssim 0.1$) for most sources (see Appendix). In the case of T04325 which lies in the middle of strong emission from the dense core L1535-NE (cf. Fig. 1j), we estimate $\epsilon_{\rm back} \simeq 0.3$.

#### 4.2.3. Non spherical envelopes, perturbation by the outflow

The millimeter dust emission of several sources is clearly not circularly symmetric but displays an elliptical or even more complex morphology (e.g. L1527, B335, HH211-MM). The asymmetries seen toward L1527 and B335 appear to be directly related to the influence of their bipolar outflows. The map of L1527 (Fig. 1l) shows a clear cross-like pattern probably marking the walls of a bipolar cavity excavated by the outflow, which is reminiscent of what is seen at 730 $\mu$m toward L1551-IRS5 (Ladd et al. 1995). The dust emission mapped around B335 is elongated perpendicular to the outflow axis (Fig. 2a). These bar-like or cross-like enhancements of 1.3 mm dust emission may originate from compression and/or heating of the envelope by the outflow (cf. Gueth et al. 1997). The resulting uncertainties can be estimated by comparing the radial profiles obtained in different quadrants of the maps (see Col. 3 of Table 4). The radial profile averaged over the northern[5] quadrant of the L1527 envelope and the profile measured perpendicular to the B335 outflow are very close to the corresponding circularly averaged profiles: $m_{\rm perp} = m_{\rm circ} \pm 0.2$. In Table 4, we thus give the power-law indices measured for the circularly-averaged intensity profiles of L1527 and B335, but add an extra $\Delta m = 0.2$ term to the uncertainty estimated from the power-law fit.

### 4.3. Assessment of the dust temperature distribution

Assuming that central heating by the inner accreting protostar dominates the thermal balance of the envelope, the dust temperature is expected to decrease outward. More precisely, one expects a radial temperature profile of the form $T(r) \propto r^{-q}$ with $q \approx 0.4$ in the region where the envelope is optically thin to the bulk of the infrared radiation (e.g. Emerson 1988; Butner et al. 1990). In practice, one thus expects (see, e.g., Terebey et al. 1993):

$$T_{\rm dust}(r, L_\star) \approx 38\ {\rm K} \times \left(\frac{r}{100\ {\rm AU}}\right)^{-0.4} \left(\frac{L_\star}{1\ L_\odot}\right)^{0.2}, \qquad (2)$$

where the stellar luminosity $L_\star$ can be approached by the bolometric luminosity listed in Table 1. Evidently, this temperature distribution is valid only up to the radius where $T_{\rm dust}(r, L_\star)$ reaches the typical dust temperature of the parent ambient cloud, i.e., $T_{\rm cloud} \sim 10$ K (appropriate to Taurus-Auriga, Perseus, and most isolated globules, see e.g. Myers & Benson 1983). The preceding equation implies that the radius, $R_{\rm isoth}$, beyond which $T_{\rm dust}(r > R_{\rm isoth}) \approx T_{\rm cloud}$, is approximately given by:

$$R_{\rm isoth}(L_\star) \simeq 2\,900\ {\rm AU} \times \left(\frac{T_{\rm cloud}}{10\ {\rm K}}\right)^{-2.5} \left(\frac{L_\star}{1\ L_\odot}\right)^{0.5}. \qquad (3)$$

The angular radius $\theta_{\rm isoth}$ corresponding to $R_{\rm isoth}$ is listed in Col. 4 of Table 4. According to these estimates, most of the envelopes observed in Taurus and isolated globules are likely to be roughly isothermal (at the temperature of the ambient cloud) on the spatial scales sampled by our maps [i.e., for $r > 1\,500\ {\rm AU} \times (d/140\ {\rm pc})$]. On the other hand, we expect central heating to play a significant role in shaping the intensity profiles of the more luminous protostars of Perseus.

For very low luminosity and/or very young accreting protostars, central heating may be completely negligible, and the envelope thermal structure may be dominated by external heating from cosmic rays and the interstellar radiation field (e.g. Goldsmith & Langer 1978; Neufeld et al. 1995), as is probably the case for pre-stellar cores. Gas-grain collisions are expected to maintain the gas and dust temperatures reasonably well coupled to each other, at least for densities $n_{\rm H2} \gtrsim 10^5\,{\rm cm}^{-3}$ (e.g. Ceccarelli et al. 1996). Calculations taking these processes into account show that externally-heated envelopes/cores are likely to be *cooler in their inner regions* than their parent ∼10 K molecular clouds (e.g. Falgarone & Puget 1985; Masunaga & Inutsuka 1999; Evans et al. 2001). Masunaga & Inutsuka (1999) find envelope temperatures of ∼6 K and ∼10 K at radii of ∼1 000 AU and ∼10 000 AU, respectively, from the center of a ∼0.1 $L_\odot$ protostar that has just entered the accretion phase. This would correspond to an effective temperature index $q \approx -0.4$ in the range of radii probed by our 1.3 mm observations. Such an outward *increase* in the envelope temperature is likely to apply to the lowest luminosity protostars of our Taurus sample, e.g., IRAM 04191 and K04166. We have thus adopted $q = -0.2 \pm 0.2$ for these objects (see Col. 5 of Table 4).

### 4.4. Inferred radial density gradients

The intrinsic intensity profiles obtained in Sect. 4.1 can now be used to constrain the radial density profiles of the observed circumstellar envelopes provided that some assumptions are made about their 3-D geometry and temperature structure (see Sect. 4.3).

For an infinite, spherically-symmetric envelope, a simple asymptotic relation exists between the column density profile (see Figs. 3,4) and the underlying radial density

[5] For unknown reasons, the L1527 envelope has a steeper intensity profile in the south-west part than along the outflow axis (cf. Fig. 1l).

gradient (e.g. Arquilla & Goldsmith 1991; YC91; Adams 1991): $N_{\rm H2}(\bar{r}) \propto r \times \rho(r)$. Consequently, in the Rayleigh-Jeans regime, spheroidal envelopes with power-law density and temperature gradients (i.e., $\rho(r) \propto r^{-p}$ and $T(r) \propto r^{-q}$, respectively) are expected to have specific intensity profiles of the form $I(\bar{r}) \propto \bar{r}^{-m}$ with $m = p+q-1$ as a function of projected radius $\bar{r}$. The power-law density index, $p = m + 1 - q$, derived in this way from the "best-fit" index of the radial intensity profile, $m$, is given in Col. 6 of Table 4, assuming the temperature index $q$ listed in Col. 5. Given the morphologies observed in the plane of the sky (see Figs. 1–2), the assumption that the envelopes are roughly spheroidal should be adequate, at least as a first approximation (see, however, Sect. 4.2.3 above and Col. 9 of Table 4). Even in the case of an ellipsoidal envelope, our approach should still yield a correct estimate for the angle-averaged density profile. On the other hand, the density and temperature gradients in the envelopes may not be correctly described by single power-laws over the full range of radii sampled by our observations. If, instead, the density and temperature gradients are represented by series of broken power-laws, then the preceding, simple formula relating $p$, $m$, and $q$ will no longer be strictly valid in the transition regions owing to convergence effects. A correction term must be added: $p = m + 1 - q - \epsilon_{\rm proj}$. In particular, this is the case for a *finite-sized* sphere where the density drops to 0 beyond some radius $R_{\rm out}$ (e.g. Arquilla & Goldsmith 1985; YC91). Our maps indicate that $\theta_{\rm out} \gtrsim 70''$ (i.e. $R_{\rm out} \gtrsim 10\,000$ AU at 140 pc) may be a typical value for the outer radius of protostellar envelopes in Taurus and Bok globules (see Col. 7 in Table 4). The correction term due to deprojection effects is then small ($\epsilon_{\rm proj} \approx 0.1$, see Appendix) and is partly compensated for by the presence of background emission (see Sect. 4.2.2). In these cases, we have thus neglected $\epsilon_{\rm proj}$ and have conservatively estimated the error bar on $p$ as $\Delta p = \Delta m + \Delta q + 0.1$. For the protostars with compact envelopes (i.e., $\theta_{\rm out} \lesssim 40''$ in Col. 2 of Table 4), we have used $\epsilon_{\rm proj} \approx 0.3$ (or 0.2 when a significant background cloud exists) and $\Delta p = \Delta m + \Delta q + 0.2$ (see Col. 6 of Table 4).

Taking the various uncertainties into account (see also Sects. 4.2 and 4.3 above), the power-law index of the radial density gradient is found to be $p \sim 1.5-2$ from $r \sim 1\,000 - 5\,000$ AU to $r \sim 10\,000 - 50\,000$ AU for the spatially resolved envelopes of Taurus YSOs and Bok globules. In several cases, the power-law density structure appears to break down at a finite radius beyond which the envelope merges with the ambient cloud: $\overline{R_{\rm out}} \gtrsim 10\,000$ AU for the Taurus YSOs and $\overline{R_{\rm out}} \gtrsim 16\,000$ AU for the Bok globules. The power-law density analysis is more uncertain for the compact protostellar envelopes of Perseus for which we estimate $p = (2 - 2.5) \pm 0.6$ and $\overline{R_{\rm out}} \sim 10\,000$ AU. For the "peculiar" Class I sources which are essentially unresolved in our maps (see Fig. 3g and Col. 7 of Table 2), the radius of any envelope, if present at all, must be much smaller, $R_{\rm out} \lesssim 1\,500$ AU. The nature of these peculiar Class I sources is discussed in Sect. 5.2.3 below.

## 5. Discussion

### 5.1. Structure of protostellar envelopes and comparison with collapse models

The millimeter continuum maps and radial profiles presented in Sects. 3 and 4 allow us to test, in Sect. 5.1.2 below, several theoretical predictions which we first summarize in Sect. 5.1.1.

#### 5.1.1. Detailed model predictions

In the self-similar collapse theory of Shu and co-workers, the instantaneous structure of a protostellar dense core is primarily determined by the position of the expansion wavefront (see Sect. 1). For a typical cloud temperature $T_{\rm cloud} \approx 10$ K (e.g. Myers & Benson 1983), the isothermal sound speed is $a_{\rm s} = \sqrt{\frac{k_{\rm B}\, T_{\rm cloud}}{\mu\, m_{\rm H}}} \simeq 0.19$ km s$^{-1}$ (where $k_{\rm B}$ is the Boltzman constant, $\mu = 2.33$ the mean molecular weight, and $m_{\rm H}$ the mass of atomic hydrogen). At the distance of the Taurus cloud, the head of the expansion wave should be located at angular radii $\theta_{\rm inf} \sim 3''$, $\sim 30''$ and $\sim 5'$, when $t = 10^4$ yr, $t = 10^5$ yr, and $t = 10^6$ yr, respectively. A power-law density profile of the form $\rho(r) \propto r^{-p}$ is expected, with $p \approx 1.5$ inside the expansion wavefront, and $p \approx 2$ further out.

More generally, the work of Whitworth & Summers (1985) shows that, during the protostellar phase (i.e., $t \geq 0$), *all* isothermal similarity solutions converge at small radii toward a free-fall density profile of the type $\rho(r,t) = \frac{1}{4\pi}\,(\dot{M}_{\rm acc}/2G)^{1/2}\, r^{-3/2}\, t^{-1/2}$, where $\dot{M}_{\rm acc} = w_0\, {a_{\rm s}}^3/G$ is the accretion rate with $w_0$ ranging from 0.975 for the Shu case to $\sim$47 for the Larson-Penston case[6].

Hence, in all self-similar isothermal models, the mass enclosed within a given radius of the infall envelope should roughly scale as $M_{\rm env}(r < R) \propto t^{-1/2}$, where $t$ is the age of the central protostar (i.e., the time elapsed since point mass formation). When the sound speed is $a_{\rm s} = 0.19$ km s$^{-1}$, the envelope masses predicted by the Shu model are: $M_{\rm env}(r < 4\,200$ AU$, t = 10^4\,{\rm yr}) \simeq 0.35\ M_\odot$, $M_{\rm env}(r < 4\,200$ AU$, t = 10^5\,{\rm yr}) \simeq 0.19\ M_\odot$, and $M_{\rm env}(r < 4\,200$ AU$, t = 10^6\,{\rm yr}) \simeq 0.03\ M_\odot$ (see e.g. Fig. 5a). For $t > 0$, the envelope masses are expected to be a factor $\sim$7 larger in the Larson-Penston solution than in the Shu model. For comparison, at point mass formation ($t = 0$), the mass enclosed by the (static) SIS at $T_{\rm cloud} = 10$ K is $M_{\rm SIS}(r < R) = \frac{2\,{\rm a}^2}{\rm G}\,{\rm R} \simeq 0.37\ M_\odot$ for $R = 4\,200$ AU, while the mass enclosed by the (dynamic) Larson-Penston flow is $\sim$4.4 times larger. In the magnetized case, a similar overdensity factor exists between the dynamical similarity solution of Contopoulos et al. (1998) around $t = 0$ and the (equilibrium) singular isothermal

[6] Similarity solutions exist with larger values of $w_0$, up to $+\infty$ (see Fig. 2 of Whitworth & Summers 1985), which physically correspond to cloud cores strongly perturbed/compressed from the outside.

magnetic disk (see discussion in Basu 1998). When the collapse initial conditions are not self-similar but correspond to pressure-truncated Bonnor-Ebert isothermal spheres, the (inner) density profile is expected to approach that of the Larson-Penston similarity solution near point mass formation ($t \gtrsim 0$) but to relax toward the Shu density profile at later times, until the expansion wavefront reaches the finite outer radius of the cloud core (see Foster & Chevalier 1993).

In the alternative, non-isothermal description of the collapse by McLaughlin & Pudritz (1996, 1997), based on a logotropic equation of state of the type $P/P_{\rm c} = 1 + A \ln(\rho/\rho_{\rm c})$ (where $A \sim 0.2$, and $P_{\rm c}$ and $\rho_{\rm c}$ are the central values of the pressure and density), the initial conditions are taken to be a singular logotropic sphere with $\rho(r) = (AP_{\rm c}/2\pi G)^{1/2} r^{-1}$, truncated by external pressure at some outer radius $R_{\rm out}$. When the collapse of such a logotrope is initiated (by, e.g., a small increase in external pressure), the density distribution also approaches a free-fall $\rho(r) \propto r^{-1.5}$ power-law[7] inside the head of the expansion wave. The envelope mass enclosed within $R = 4\,200$ AU remains essentially constant during a first "redistribution" phase. For a critical logotrope of total mass $M_{\rm tot} \sim 92\ M_\odot$ and outer radius $R_{\rm out} \simeq 19\,000$ AU, this phase lasts for approximately $10^6$ yr and the enclosed mass is $M_{\rm env}(r < 4\,200 \text{ AU}, t = 0 - 10^6 \text{ yr}) \simeq 0.15\ M_\odot$, assuming the nominal parameters adopted by McLaughlin & Pudritz (i.e., $T_{\rm cloud} = 10$ K and a surface pressure $P_{\rm s} = 1.3\ 10^5 \times k_{\rm B}$ cm$^{-3}$ K). Thereafter, the stellar mass increases roughly as $M_\star(t) \propto t^4$ and the envelope mass decreases accordingly [$M_{\rm env}(t) = M_{\rm tot} - M_\star(t)$], until all the mass has been accreted and the accretion phase is terminated at $t \simeq 2.5\ 10^6$ yr. The accretion history predicted by this model is thus very different from that of the Shu et al. model.

### 5.1.2. Comparison with observations

Given observational uncertainties, the power-law density structure derived in Sect. 4 for the envelopes of bona-fide protostars in Taurus and Bok globules [$\rho(r) \propto r^{-p}$ with $p \simeq 1.5 - 2$] is consistent with that expected for either a SIS ($p = 2$) or a free-fall configuration ($p = 1.5$). In the context of the standard protostellar model, the median circumstellar mass $\overline{M_{\rm env}^{4200\ \rm AU}} \lesssim 0.074\ M_\odot$ estimated for our complete sample of Taurus candidate protostars corresponds to a collapse age of $t \gtrsim 3\ 10^5$ yr. This value is in rough agreement with the typical lifetime inferred for Taurus Class I sources based on statistical arguments ($t \simeq 1 - 2\ 10^5$ yr – see, e.g., KHSS90). Furthermore, the median envelope mass of the "bona-fide" Class I/0 protostars of Taurus, $\overline{M_{\rm env}^{4200\ \rm AU}} \sim 0.28\ M_\odot$, is within a factor of $\lesssim 2$ of $M_{\rm SIS}(r < 4\,200\,\text{AU})$, suggesting that these objects are still well into the main accretion phase with estimated collapse ages $t \lesssim 5\ 10^4$ yr. By contrast, the median mass measured for the 11 undetected or unresolved Class I sources of Taurus (see e.g. Fig. 3g), is very low ($\overline{M_{\rm env}^{4200\ \rm AU}} < 0.01\ M_\odot$), and corresponds to a very old collapse age $t \gtrsim 9\ 10^6$ yr. This is much longer than the estimated lifetime of the protostellar embedded phase, implying that the peculiar Class I sources cannot be genuine protostars. Altogether, except perhaps for these peculiar sources (see also Sect. 5.2.1 below), our Taurus results are in fairly good agreement with the predictions of the standard collapse model.

On the other hand, the envelopes of Class 0 protostars in both Perseus and isolated globules tend to be a factor of ∼2 to ∼12 *more massive* than is predicted by the standard model, even if very young collapse ages are assumed: $M_{\rm env}^{4200\ \rm AU} \simeq 0.6 - 5\ M_\odot$ is measured, while a maximum of $M_{\rm SIS}(r < 4\,200 \text{ AU}) \simeq 0.4\ M_\odot$ is expected. As the gas temperature in the initial cloud core cannot be much larger than 10 K (e.g. Ladd et al. 1994), such large masses cannot be explained in the SIS picture unless non-thermal sources of support are included. A factor of ∼2 increase in mass can be accommodated by the standard model if a significant (static) magnetic field is present (e.g. Li & Shu 1996). In principle, turbulence may also contribute to the support of the initial dense core (e.g. Myers & Fuller 1992). However, the small-scale condensations or "kernels" corresponding to the progenitors of protostars in star-forming clusters (e.g. MAN98) appear to be essentially "coherent", i.e., largely devoid of turbulence (Goodman et al. 1998; Myers 1998; Belloche et al. 2001). We conclude that variants of the standard model can probably account for the masses measured in most Bok globules but are clearly insufficient to explain the $> 1.5\ M_\odot$ envelopes observed toward L1157-MM and the Class 0 objects of Perseus. The most likely explanation in the latter cases is that the collapse started from non-singular initial conditions, resulting in a nonequilibrium density configuration similar to the Larson-Penston flow near point mass formation (see Sect. 5.1.1 above). Such a conclusion, which is consistent with the large accretion/ejection rates inferred for Perseus Class 0 objects (Bontemps et al. 1996 – hereafter BATC96), could be tested if direct observational constraints on the infall velocity field of these sources are obtained: large infall velocities are indeed expected.

In contrast to isothermal models, the logotropic model of McLaughlin & Pudritz (1997) accounts only marginally for our Taurus results: the radial density structure we observe ($p \simeq 1.5 - 2$) is somewhat steeper than the predictions (i.e., $p = 0.5 - 1.5$). The disagreement is most serious for the Taurus YSOs with the most massive envelopes, namely the young Class 0 objects IRAM 04191, K04166, and L1527, which have $p = (1.8 - 2.2) \pm 0.5$, while $p = 0.5 - 1$ is expected at $t \lesssim 10^6$ yr in this model. Moreover, the envelope mass predicted by the nominal

[7] There is, however, a transition region just inside the expansion wavefront where the density gradient is flatter and closer to $\rho(r) \propto r^{-0.5}$.

critical model of McLaughlin & Pudritz during the collapse [$M_{\rm env}(r < 4\,200$ AU) $\lesssim 0.15\ M_\odot$ at most] is significantly lower than that implied by our observations in both Taurus and isolated globules. The case of B335 is discussed by McLaughlin & Pudritz (1997) who conclude that this object may correspond to a 1 $M_\odot$ collapsing logotrope at the end of its accretion phase. However, our measurements of the envelope mass [$M_{\rm env}^{4200\ \rm AU} \simeq 0.9\ M_\odot$][8] and power-law density index [$p = 2.2 \pm 0.4$] are not consistent with such a model which predicts $M_{\rm env}(r < 4\,200$ AU) $\ll 0.034\ M_\odot$ and $p = 1.5$.

Furthermore, none of the low-mass *pre-stellar* cores studied in detail up to now has a density structure consistent with a pressure-truncated logotrope (Bacmann et al. 2000).

### *5.2. Protostellar evolution in Taurus-Auriga*

#### 5.2.1. The $M_{\rm env} - L_{\rm bol}$ evolutionary diagram

As shown by AM94 and Saraceno et al. (1996), the envelope mass ($M_{\rm env}$) vs. bolometric luminosity ($L_{\rm bol}$) diagram can be used as a practical evolutionary diagram for embedded YSOs. While $M_{\rm env}$ provides a measure of the mass reservoir that remains to be accreted, the bolometric luminosity $L_{\rm bol}$ may be used to estimate the mass of the central star, $M_\star$, via plausible mass–luminosity relations for protostars (see AM94 for details). Conceptually, Class 0 protostars were defined as YSOs with $M_{\rm env} > M_\star$ by AWB93. Because of uncertainties in, e.g., the mass–luminosity relationship, the actual observational boundary between Class 0 and Class I objects is not a well-defined border line but a border zone. The original Class 0 criterion given by AWB93, namely $L_{\rm submm}^{\lambda > 350\ \mu\rm m}/L_{\rm bol} > 0.5\%$, is based on a linear mass–luminosity relationship (i.e., $M_\star \propto L_{\rm bol}$, as expected if $L_{\rm bol}$ derives only from accretion onto a star with a fixed $\dot{M}_{\rm acc}/R_\star$ ratio) and typical dust properties for converting $L_{\rm submm}^{\lambda > 350\ \mu\rm m}$ to $M_{\rm env}$ (cf. AWB93 and AM94). In terms of the $M_{\rm env}$–$L_{\rm bol}$ diagram, this roughly corresponds to $M_{\rm env}/L_{\rm bol} > 0.1\ M_\odot/L_\odot$. In practice, the status of sources lying close to this formal border line is uncertain, and only YSOs with $L_{\rm submm}^{\lambda > 350\ \mu\rm m}/L_{\rm bol} >> 0.5\%$ are considered as bona-fide Class 0 objects (see AWB2000).

Our $M_{\rm env}$–$L_{\rm bol}$ diagram for the embedded YSOs of Taurus is displayed in Figs. 5a,b, along with two sets of evolutionary tracks. The values of $M_{\rm env}$ (from Sect. 3.2) and $L_{\rm bol}$ (from the literature) used in this diagram can be found in Tables 1 and 2, respectively. Rather than the total masses detected in the maps, we have preferred to use our estimates of the inner envelope mass, $M_{\rm env}^{4200\ \rm AU}$ (see Sect. 3.2). Our maps suggest that the envelopes of bona-fide protostars in Taurus have a power-law density structure up to a fairly large radius, $R_{\rm out} \sim 4\,000$–$17\,000$ AU (cf. Col. 7 of Table 4). But the total mass measured within

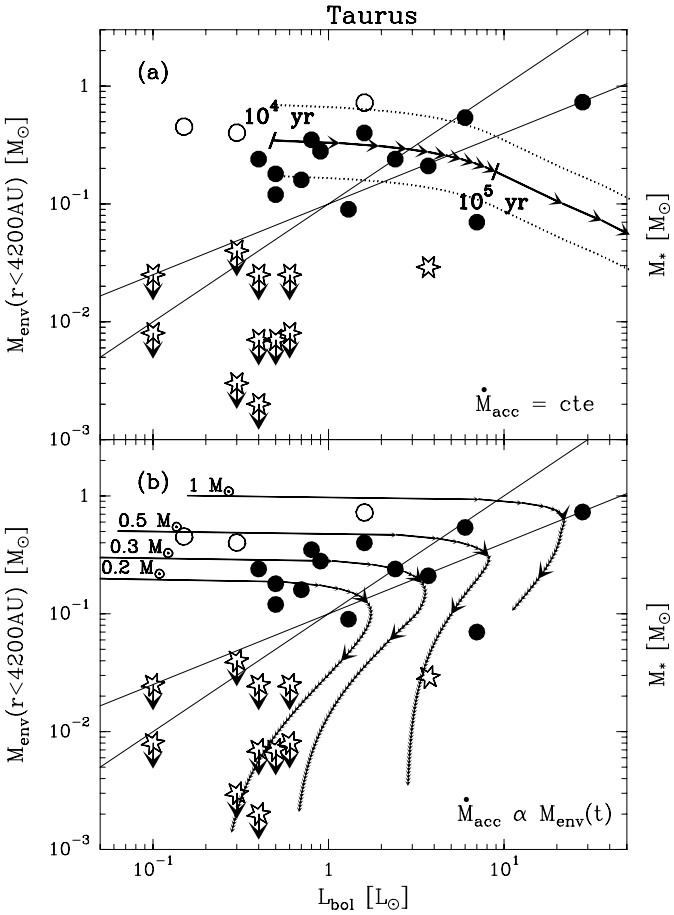


**Fig. 5.** $M_{\rm env}^{4200\ \rm AU}$ vs. $L_{\rm bol}$ diagram in Taurus. Bona-fide protostars are shown as (open and filled) circles (for Class 0 and Class I objects, respectively), while peculiar Class I sources are denoted by open star-like markers. The solid straight lines are two $M_\star$–$L_{\rm bol}$ relations marking the conceptual border zone between the Class 0 stage ($M_{\rm env}^{4200\ \rm AU} > M_\star$) and the Class I stage ($M_{\rm env}^{4200\ \rm AU} < M_\star$): $M_\star \propto L_{\rm bol}$ (cf. AWB93 and AM94) and $M_\star \propto {L_{\rm bol}}^{0.6}$ as suggested by the time-dependent accretion scenario of the text (see also AWB2000). Two distinct sets of evolutionary tracks (solid curves) are shown, based on: **a)** A constant accretion rate, $\dot{M}_{\rm acc} \approx 2\ 10^{-6}\ M_\odot\ {\rm yr}^{-1}$, as in the standard model. Arrows mark time steps from $t = 10^4$ yr to $t = 4 \times 10^5$ yr. (The dotted curves illustrate the magnitude of the observational uncertainties on $M_{\rm env}^{4200\ \rm AU}$.) **b)** A time-dependent accretion rate, $\dot{M}_{\rm acc} \propto M_{\rm env}(t)$, as described in the text. Small arrows are plotted on the tracks every $10^4$ yr, big arrows when 50% and 90% of the initial core mass has been accreted

$R_{\rm out}$, which has a median value $\overline{M_{c\star}^{R_{\rm out}}} \sim 0.83\ M_\odot$, is unlikely to be entirely accreted by the central object. As pointed out by, e.g., Ladd et al. (1998), the outflow will probably disperse a significant fraction of this mass. Our map of the L1527 envelope, which shows some evidence for a bipolar cavity oriented along the outflow axis (Fig. 1l), is consistent with this view. As the star formation efficiency in a single isolated core is expected to be ∼30% on theoretical grounds (Matzner & Mckee 2000), we believe that the initial core mass within $R = 4\,200$ AU should provide

[8] The measured envelope mass also exceeds by a factor of $> 3$ that of the best-fit inside-out isothermal collapse model of Choi et al. (1995).

a better indicator of the final stellar mass than the total core mass.

The first set of evolutionary tracks, shown in Fig. 5a, corresponds to the predictions of the standard protostellar model (e.g. Adams et al. 1987) and assumes that $L_{\rm bol} = L_{\rm acc} = (G\,M_\star\,\dot{M}_{\rm acc})/R_\star$, with $a_{\rm s} = 0.19$ km s$^{-1}$ (i.e., $\dot{M}_{\rm acc} \simeq 1.6\ 10^{-6}\ M_\odot\ {\rm yr}^{-1}$) and $R_\star = 3\ R_\odot$.

The second set of evolutionary tracks (Fig. 5b) shows the predictions of the accretion scenario advocated by BATC96 and AWB2000, in which protostars form from dense cores with *finite* initial masses, $M_0$, and both the envelope mass and the accretion rate are assumed to decline exponentially with time according to $\dot{M}_{\rm acc}(t) = M_{\rm env}(t)/\tau = M_0\ \exp(-t/\tau)/\tau$, where $\tau \approx 10^5$ yr is a characteristic time. Such a decline of $\dot{M}_{\rm acc}$ is consistent with the decrease of outflow power observed from Class 0 to Class I protostars (BATC96), and is theoretically expected in the case of non-singular collapse initial conditions (e.g. Foster & Chevalier 1993; HAB97). The tracks of Fig. 5b further assume that the observed bolometric luminosities result from a combination of accretion and stellar contributions: $L_{\rm bol} = GM_\star\dot{M}_{\rm acc}/R_\star + L_\star$, where $R_\star(M_\star, \dot{M}_{\rm acc}) \approx 3\,R_\odot$ is the stellar radius and $L_\star(M_\star, \dot{M}_{\rm acc})$ the stellar luminosity on the birthline for PMS stars[9] (Stahler 1988).

It can be seen that the "standard" tracks based on the self-similar theory of Shu et al. (1987) account relatively well for the locations of the bona-fide protostars of Taurus in the $M_{\rm env}$–$L_{\rm bol}$ diagram (see Fig. 5a). Furthermore, there is a good continuity between Class 0 and (bona-fide) Class I objects: In regions of isolated star formation, Class 0 objects (open circles in Fig. 5a) may merely correspond to extreme versions of bona-fide Class I sources (filled circles). A similar conclusion was reached by HAB97 based on a discussion of the outflow properties (see Fig. 10 of HAB97). In this respect, it is noteworthy that more than half of the bona-fide Class I sources of Fig. 5 lie *above* the solid straight lines marking the border zone between $M_{\rm env}^{4200\ {\rm AU}} > M_\star$ and $M_{\rm env}^{4200\ {\rm AU}} < M_\star$ in the diagram: They match the conceptual definition of the Class 0 stage given by AWB93 (see above). Our observations are thus consistent with the idea that *all* of the bona-fide Class 0 and Class I objects of Fig. 5 are in the main accretion phase of YSO evolution.

Despite this reasonably good agreement, two problems should be pointed out. First, as noticed by Kenyon et al. (1993a, hereafter KCH93) and summarized by Hartmann (1998), the accretion luminosities predicted by the standard model tend to be larger than the observed bolometric luminosities by up to an order of magnitude: the luminosity predicted at a typical collapse age of $\sim$2 $10^5$ yr is $L_{\rm acc} \sim 5\,L_\odot$, while the median Class I/0 luminosity in our sample is $\overline{L_{\rm bol}} \sim 0.8\,L_\odot$. This discrepancy is quite severe even though it can be reduced by a factor of $\lesssim 2$ if non-spherical accretion effects and wind driving are properly taken into account (cf. Shu et al. 1996). The solution proposed by KCH93 is that envelope material does not fall directly onto the central star but piles up in a disk whose radius is substantially larger than the stellar radius, thereby reducing the infall luminosity. It remains to be seen, however, whether short episodes of high disk accretion ("FU Ori" outbursts) can be made frequent enough to maintain $M_{\rm disk} \lesssim 0.1\,M_\odot$ throughout the embedded phase, as measured by millimeter interferometers (e.g. Terebey et al. 1993; Looney et al. 2000).

A second problem with the evolutionary tracks of the standard model is that they do not account for the properties of the peculiar Class I sources identified here (open star markers in Fig. 5a). In spite of their Class I infrared SEDs (Adams et al. 1987; KCH93) and low bolometric temperatures ($\overline{T_{\rm bol}} = 350$ K according to Chen et al. 1995), these objects *cannot* be interpreted as accreting protostars in the framework of the inside-out collapse model. Possible interpretations are given in Sect. 5.2.3 below.

The tracks assuming an exponential decrease in the rate of envelope dissipation with time (Fig. 5b) explain the luminosities of the bona-fide Class 0/I protostars better than do the standard tracks (see also HAB97 and Myers et al. 1998), and account even marginally for the locations of the peculiar Class I sources.

Although obviously idealized, this time-dependent accretion scenario hints that the peculiar Class I sources may correspond to low-mass objects at the very end of the protostellar accretion phase. In this view, they would be the descendants of the lowest mass bona-fide protostars of Fig. 5. Physically, an exponential termination of the accretion phase may result from the finite mass reservoir available in the initial pre-collapse core. Indeed, our 1.3 mm continuum maps suggest that, even in Taurus, the initial core is bounded with $R_{\rm out} \gtrsim 10\,000$ AU (see, e.g., Fig. 3f). When the collapse expansion wave reaches $R_{\rm out}$ (which occurs at $t = R_{\rm out}/a_{\rm s} \gtrsim 2.5\ 10^5$ yr in the standard picture), the circumstellar evolution is likely to change drastically in character: the central YSO should enter a phase of residual accretion and its remnant envelope may be quickly dispersed by the outflow. The peculiar Class I sources may be representative of this late accretion phase.

### 5.2.2. Comparison with $\rho$ Ophiuchi

For direct comparison with Fig. 5, we show in Fig. 6 the $M_{\rm env}$–$L_{\rm bol}$ diagram constructed for the self-embedded YSOs of $\rho$ Ophiuchi using data from AM94, MAN98, and Wilking et al. (1989). Since the protostars of $\rho$ Ophiuchi are surrounded by compact, finite-sized envelopes (cf. MAN98), $M_{\rm env}$ is here simply taken to be the total mass enclosed within a relatively well-defined envelope outer radius (cf. AM94). The same evolutionary tracks as in Fig. 5 are superposed. In this case, a clear contrast

[9] As the precise position of the birthline depends on $\dot{M}_{\rm acc}$, both $R_\star$ and $L_\star$ were interpolated from the values given by Stahler (1988) for constant accretion rates of 2 $10^{-6}\ M_\odot\ {\rm yr}^{-1}$ and $10^{-5}\ M_\odot\ {\rm yr}^{-1}$.

between Class 0 and Class I objects is apparent. The standard tracks, which would imply a continuum of protostars rather than two separate classes, do not fit the $\rho$ Oph diagram and cannot account for the observed Class I sources with $M_{\rm env} \lesssim 0.1\,M_\odot$ and $L_{\rm bol} \sim 1$–$2\,L_\odot$.

On the other hand, the time-dependent accretion tracks explain all of the $\rho$ Oph objects reasonably well. It is also noteworthy that the sources are on average more luminous (by a factor ∼3–10) in Ophiuchus than in Taurus (see also Chen et al. 1995). This, coupled with the fact that the standard accretion scenario is satisfactory in Taurus, supports the suggestion of HAB97 (see also André 1997) that embedded YSOs follow different accretion histories in $\rho$ Ophiuchi and in Taurus. This is presumably the result of a marked difference in fragmentation lengthscale between the two clouds: $R_{\rm out} \sim 3\,000$ AU in $\rho$ Oph (cf. MAN98) versus $R_{\rm out} \gtrsim 10\,000$ AU in Taurus (this paper).

Comparing Fig. 5 with Fig. 6, and Fig. 1 with the $\rho$ Oph 1.3 mm maps of AM94 and MAN98, we suggest that the circumstellar evolutionary state of the peculiar Class I YSOs of Taurus may be similar to that of the typical Class I sources of Ophiuchus: in both cases, only remnant, compact envelopes are present.

### 5.2.3. Nature of the unresolved Class I sources

A possible interpretation of the peculiar Class I objects is that they are in fact PMS stars seen in a particular configuration and/or environment. The very weak, if not absent, outflow activity observed toward the peculiar Class I sources (see BATC96) supports this view. First, some of these sources may be viewed through a high visual extinction due to a large inclination to the line of sight (cf. Sonnhalter et al. 1995). Existing near-infrared maps of scattered light toward K04302 show a pronounced dark lane and are indeed suggestive of a TTS surrounded by a circumstellar disk seen roughly edge-on (Padgett et al. 1999; see also Lucas & Roche 1997). Second, a PMS star with a very low envelope mass could also present a Class I SED if its disk is warped by the tidal effects of a close companion (Terquem & Bertout 1993, 1996). Possible examples of this could be M04108-B, M04295, and M04489, whose estimated extinctions are moderate and which appear point-like in near-infrared images (Kenyon et al. 1993b). Third, several sources, such as M04108-B, Elias6, and HH30-IRS, are observed on the same line of sight as diffuse cloud emission (see Col. 8 of Table 2). This may produce both substantial near-IR extinction and significant far-IR (IRAS) excess resulting in a Class I SED.

On the other hand, the near-infrared spectra observed by Greene & Lada (1996) for L1489, M04295, M04489 and M04181+2655 differ from those of T Tauri stars. If the near-IR spectroscopy scheme developped by Greene & Lada (1996) is correct, M04295, M04489 and M04181+2655 should be intermediate objects between protostars and PMS stars and L1489 should be surrounded by significant envelope material. We also note that Z04260

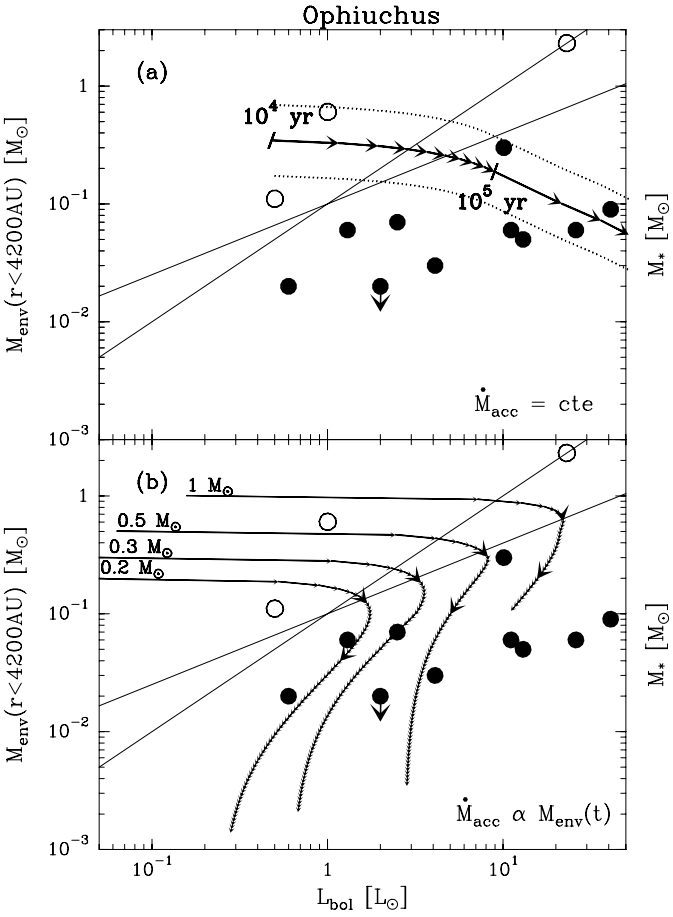


**Fig. 6.** Same as Fig. 5 for the embedded YSOs of the $\rho$ Ophiuchi main cloud (adapted from AM94). In this case, $M_{\rm env}^{4200\ {\rm AU}}$ is equivalent to the *total* envelope mass $M_{\rm env}$. Note that, in contrast to the Taurus diagram, there is a gap between Class 0 and Class I objects here

is not strictly point-like in our 1.3 mm data (see Fig. 11k). Furthermore, millimeter interferometric mapping of L1489 (e.g. Hogerheijde et al.1997, 1998; Ohashi 1999) reveals a ∼1 000 AU rotating structure with possible infall motions, which is apparently different from the more compact disks typically observed in T Tauri stars (see, e.g., Dutrey et al. 1996).

Several peculiar Class I sources may thus be highly reddened PMS stars while others could be objects in transition between protostars and T Tauri stars. These sources illustrate that the interpretation of YSO SEDs is non unique and that mapping information, preferably at several wavelengths, is crucial to get at a proper physical picture (see also Miroshnichenko et al. 1999).

### *5.3. Cold dense fragments undetected by IRAS*

As mentioned in Sect. 3, our 1.3 mm maps reveal the presence of at least seven new dense cores/condensations in the vicinity of the targeted YSOs (see Table 3). Since these cold cores do not coincide with IRAS point sources, they are good candidates for being at either the pre-stellar

stage or the Class 0 protostellar stage of evolution (cf. AWB2000). One of these objects, IRAM 04191, has been studied in more detail (AMB99) and corresponds to the first clear-cut example of a Class 0 protostar in Taurus: It has a large envelope mass ($M_{\rm env}^{4200\ {\rm AU}} \sim 0.5\,M_\odot$), very low bolometric luminosity and bolometric temperature ($L_{\rm bol} \sim 0.15\,L_\odot$, $T_{\rm bol} \sim 18\,{\rm K}$), and features a jet-like CO outflow as well as extended infall motions. Some of the cores of Table 3 may also be associated with very young accreting protostars. On the other hand, the fact that five of these sources have flat inner intensity profiles (see Sect. 4.1 and Fig. 3h) suggests that they rather correspond to pre-stellar dense cores similar to those discussed by Ward-Thompson et al. (1994, 1999). Follow-up observations are required to assess their nature more firmly. In any event, the serendipitous discovery of these cold objects in the course of a pointed 1.3 mm mapping study of IRAS YSOs clearly emphasizes the need for deep, unbiased surveys of molecular clouds in the submillimeter band. Such surveys should soon become possible with, e.g., the Far InfraRed and Submillimeter Telescope (FIRST) of ESA.

## 6. Summary and conclusions

In an effort to constrain protostellar evolution and test the predictions of collapse models, we have mapped the column density structure of the circumstellar environment of 49 low-mass embedded YSOs in the dust continuum at 1.3 mm. Our sample includes all 27 Class I (and Class 0) sources presently known in Taurus, along with 9 isolated Bok globules and 9 protostars in Perseus. Our main findings may be summarized as follows:

1. In good agreement with the predictions of the standard protostellar model of Shu et al. (1987), 16 of the Taurus Class I/0 sources are observed to be surrounded by relatively massive ($\overline{M_{\rm env}^{4200\ {\rm AU}}} \sim 0.3\ M_\odot$), spatially extended ($R_{\rm out} \gtrsim 10\,000$ AU) circumstellar envelopes with a power-law density gradient such as $\rho(r) \propto r^{-2}$ or $\rho(r) \propto r^{-1.5}$. These sources are consistent with being "bona-fide" protostars, currently in their main accretion phase;
2. Contrary to expectations, however, the 1.3 mm continuum emission mapped toward 11 Class I sources in Taurus and 1 Class I Bok globule is weak and essentially unresolved. These "peculiar" Class I sources have very small circumstellar envelope masses, $M_{\rm env}^{4200\ {\rm AU}} <$ 0.002–0.04 $M_\odot$, implying that they cannot be genuine protostars and must be at the very end of their accretion phase. Despite their low bolometric temperatures ($\overline{T_{\rm bol}} \sim 350$ K), they are most likely highly reddened PMS stars and/or transition objects between protostars and T Tauri stars;
3. Like the "bona-fide" protostars of Taurus, 8 of the 9 embedded YSOs mapped in Bok globules have circumstellar envelope properties that are consistent to first order with the standard model. The envelopes of these objects tend nevertheless to be a factor of ∼2 denser than is predicted by a purely thermal model with $T_{\rm cloud} = 10$ K. Magnetic fields may have contributed a significant fraction of the support in the corresponding pre-collapse cloud cores;
4. By contrast, the envelopes of 8 Class 0 protostars in Perseus are found to be much denser, by a factor of 3–12, than is expected in the standard collapse model. They are also relatively compact with outer radii of only a few thousand AUs ($R_{\rm out} \sim 10\,000$ AU). This is suggestive of a more dynamical picture in which external disturbances initiate the collapse of finite-sized cloud fragments with flat inner density profiles, and supersonic infall velocities develop during a runaway isothermal phase prior to the main accretion stage. Such a picture appears to be more appropriate than the standard model for describing individual collapse in cluster-forming cores. Direct spectroscopic measurements of the velocity field are however needed to confirm this view;
5. In the close environment of 6 of the 24 Class I YSOs mapped in Taurus, our maps revealed the presence of previously unknown 1.3 mm continuum condensations. All are undetected in the infrared and are good candidates for being new pre-stellar cores and/or young accreting protostars. One of them coincides with the Class 0 object IRAM 04191 already discussed in AMB99. The discovery of these cold condensations shows that infrared observations can only give a partial census of star formation activity in molecular clouds (see also point 2 above), and emphasizes the need for deep, unbiased mapping surveys in the submillimeter band.

*Acknowledgements.* We would like to thank Roberto Neri for providing the observing parameters necessary to develop our simulation program within the NIC software. We also acknowledge the participation of Sylvie Cabrit in the early phases of this work and the contribution of Sylvain Bontemps during the last observing run. We are also grateful to Anne Dutrey, Frédéric Gueth, Stéphane Guilloteau, and Roberto Neri for their assistance in deriving disk fluxes from our Plateau de Bure interferometric observations.

## Appendix: Simulations of dual-beam scanning observations with the bolometer array

We have developed a program that simulates, for any given input model envelope, the dual-beam maps that would be observed by the various channels of the bolometer array in the on-the-fly scanning mode. For each source, the simulation procedure uses the same "mapping geometry" as in the real observations: same map size, integration steps (in both azimuth and elevation), absolute coordinates of map center, observing hour angle, wobbler throw, and array geometry. The procedure also accounts for any possible offset of the source with respect to map center and includes a convolution with the beam of the telescope. The simulated dual-beam maps are then reduced in exactly the same way as the real data, including baseline subtraction, flagging

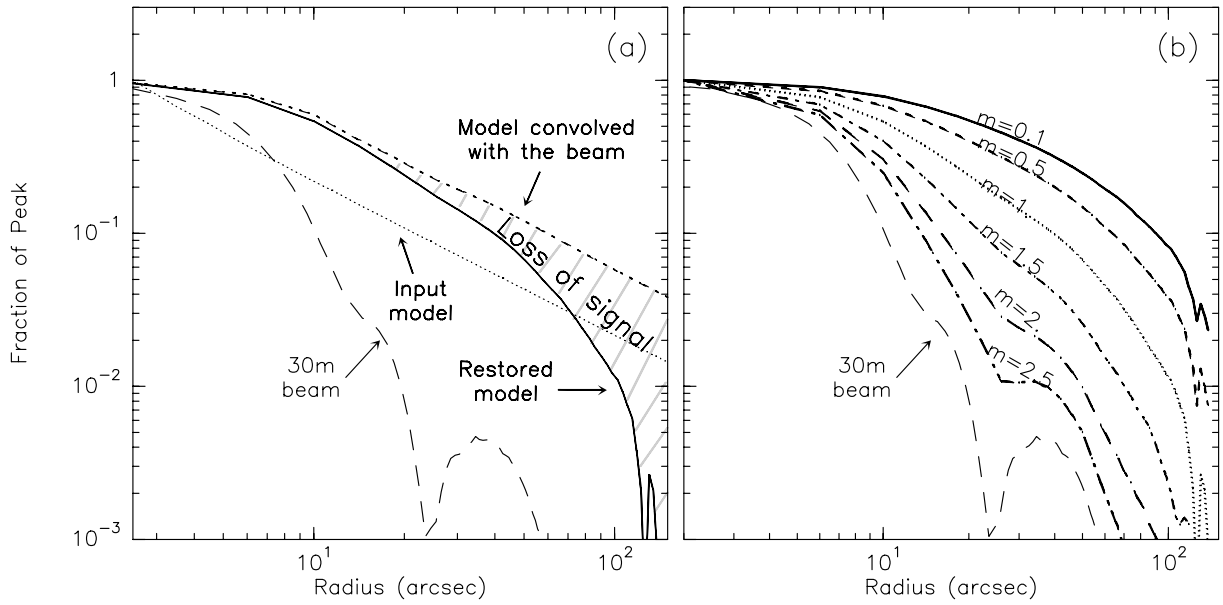


**Fig. 7. a)** Effect of the dual-beam observing technique on the observed radial intensity profiles. The dash-dotted curve represents an input model with $I(\theta) \propto \theta^{-1}$ (cf. dotted line) after convolution with the beam of the telescope (dashed curve). The solid curve shows the output model profile that results from our simulation of the dual-beam observation and the various data reduction steps. **b)** Grid of simulated profiles for a range of input power-law models, $I(\theta) \propto \theta^{-m}$, with $m = 0.1$ to 2.5

of any bad channel, restoration to equivalent single-beam Az-El maps, and combination/projection onto a RA-Dec grid (see, e.g., Emerson et al. 1979; Broguière et al. 1995).

These simulations allow us to assess the loss of signal which results from observing extended envelopes with the dual-beam method. As an example, Fig. 7a shows the transformation of a $I(\theta) \propto \theta^{-1}$ input envelope model (dotted line) after convolution with the 30 m beam (dashed-dotted line) and the various observation/data reduction steps (solid line). For such an extended envelope model, the beam convolution does not modify the slope of the profile at angular radii $\theta > HPBW$ (i.e., $11''$ here), in agreement with the conclusions of Adams (1991). However, the observation/data reduction technique does change the shape of the radial profile (see hatched region in Fig. 7a), due to the finite size of the maps. This is because all spatial scales larger than the azimuth extent $\Delta Az$ of the maps are filtered out. The slope of the simulated output profile depends only weakly on the value of the wobbler throw as long as the latter remains small compared to the map size (in azimuth). (Note that the chop throw would be the most determinant factor in the case of on-off/jiggle-stare maps.) The array geometry and the offset of the source model with respect to map center have little influence on the simulated profile providing the map is big enough that the source is effectively imaged as a positive and a negative signal by each bolometer. Baseline subtraction also has a negligible effect as long as only low-order polynomials are taken out, namely a baseline of order 0–2 applied in time on the global image, plus a simple DC level (0-order baseline) on each map row.

Figure 7b presents a grid of simulated model profiles based on the map geometry corresponding to our observations of L1527 (see Fig. 3c). The input models have power-law profiles of the form $I(\theta) \propto \theta^{-m}$ with $m = 0.1$ to 2.5 beyond an inner radius of $\theta_{\rm in} = 0.5''$. (Note that the simulated profiles for $m < 2$ are not sensitive to the exact value of $\theta_{\rm in}$ as long as it is much smaller than the beam radius, i.e. $\theta_{\rm in} < HPBW/10$.) As expected, the shallower the slope of the input model, the larger the fractional loss of emission due to the dual-beam observing mode. It is thus crucial to estimate the level of this effect through simulations before a reliable comparison between observed profiles and input models can be made. Such a comparison is more uncertain in the case of envelopes with steep density gradients (e.g. $m \geq 2$ in Fig. 7b), as this leads to radial intensity profiles which closely follow the shape of the beam. Although the main beam of the 30 m telescope is a relatively well known Gaussian with $FWHM \simeq 11''$ at 1.3 mm, the effective error beam associated with dual-beam on-the-fly bolometer observations is more poorly characterized. In particular, the beam model proposed by Guélin (1992) from spectroscopic observations at 1 mm appears to be inconsistent with our own estimation based on bolometer mapping of strong point sources (see dashed line in Fig. 7b). Fortunately, this is not a serious problem here since the radial intensity profiles of most of our sources are well resolved and cannot be fitted by steep ($m \geq 2$) power-laws.

In order to simulate the effect of an inner disk component, we have added a central point source to a $I(\theta) \propto \theta^{-1}$ power-law envelope model (see Fig. 8a). The resulting intensity profile follows the shape of the error beam at large

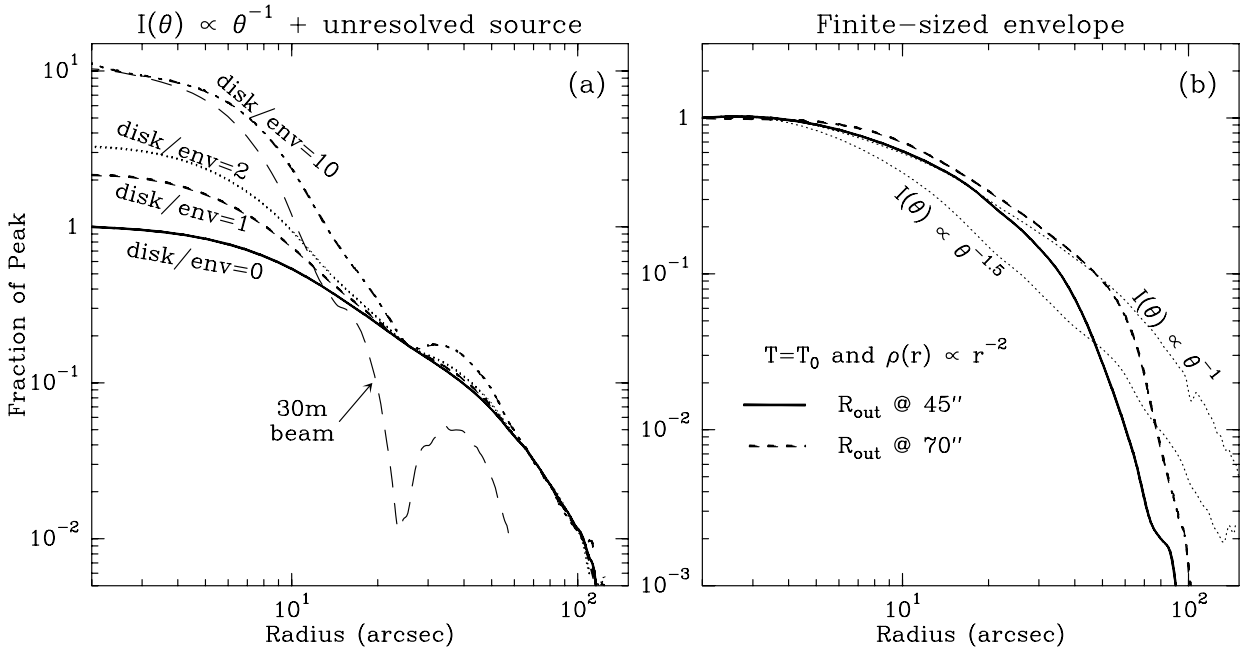


**Fig. 8. a)** Grid of simulated profiles corresponding to a $I(\theta) \propto \theta^{-1}$ input envelope model including an unresolved central source (or disk) characterized by $S_{\rm disk}/S_{\rm env}^{\rm peak} = 0$, 1, 2 and 10. **b)** Simulated profiles corresponding to finite-sized isothermal envelope models with $\rho(r) \propto r^{-2}$ inside an outer radius corresponding to $\theta_{\rm out} = 45''$ and $70''$

radii when $S_{\rm disk}/S_{\rm env}^{\rm peak} \gtrsim 5$. (For a $I(\theta) \propto \theta^{-1.5}$ input envelope model, the same occurs when $S_{\rm disk}/S_{\rm env}^{\rm peak} \gtrsim 3$.) Although such large "disk-to-envelope" ratios could apply to T Tauri stars (e.g. HL Tau), they are not observed in the case of bona-fide protostars which typically have $S_{\rm disk}/S_{\rm env}^{\rm peak} \lesssim 30\%$ (see, e.g., Looney et al. 2000; Motte et al. 2001). In most cases, the disk should thus have a negligible influence on our analysis of the envelope radial profiles at angular radii $\theta > HPBW$.

We have also embedded a $I(\theta) \propto \theta^{-1}$ envelope model in a Gaussian background cloud with $FWHM = 0.5$ pc and a cloud-to-envelope peak flux ratio of $S_{\rm cloud}^{\rm peak}/S_{\rm env}^{\rm peak} \sim 5\%$, corresponding to a typical ambient column density of $N_{\rm H2} \sim 10^{21}-10^{22}\,{\rm cm}^{-2}$. The emission of such an extended Gaussian cloud is essentially filtered out by the dual-beam observing technique. Thus, the apparent power-law index $m_{\rm obs}$ of the radial profile should only be corrected by a small term $\epsilon_{\rm back} \lesssim 0.1$ to yield the intrinsic index of the envelope profile, i.e., $m_{\rm env} = m_{\rm obs} + \epsilon_{\rm back}$ (see Sect. 4.2.2).

Finally, we have simulated the dual-beam observation of a finite-sized envelope with an outer radius $R_{\rm out}$ similar to the values measured from Figs. 3 and 4 (see Table 4). Typically, our observations suggest $R_{\rm out} \gtrsim 6 \times HPBW \simeq 30\%\ \Delta Az$ in Taurus and Bok globules, and $R_{\rm out} \gtrsim 3.5\ HPBW \simeq 18\%\ \Delta Az$ in Perseus. According to YC91, the slopes of the intensity profiles measured on such angular scales (i.e., $HPBW < \theta < 3.5-6 \times HPBW$) should be corrected by $\epsilon_{\rm proj} > 0.5$ when estimating the intrinsic slopes of the *density* profiles (i.e., $p = m+1-q-\epsilon_{\rm proj}$), in order to properly account for projection effects. Figure 8b shows that, due to dual-beam filtering, the effective correction term is much smaller in our case: $\epsilon_{\rm proj} \lesssim 0.1$ in Taurus and Bok globules and $\epsilon_{\rm proj} \simeq 0.3$ in Perseus.

## References


Adams, F. C. 1991, ApJ, 382, 544
Adams, F. C., Lada, C. J., & Shu, F. H. 1987, ApJ, 312, 788
Agladze, N. I., Sievers, A. J., Jones, S. A., Burlitch, J. M., & Beckwith, S. V. W. 1996, ApJ, 462, 1026
André, P. 1997, in Herbig-Haro Flows and the Birth of Low-Mass Stars, IAU Symposium 182, ed. B. Reipurth, & C. Bertout (Kluwer, Dordrecht), 483
André, P., & Montmerle, T. 1994, ApJ, 420, 837 (AM94)
André, P., Ward-Thompson, D., & Barsony, M. 1993, ApJ, 406, 122 (AWB93)
André, P., Ward-Thompson, D., & Barsony, M. 2000, in Protostars and Planets IV, ed. V. Mannings, A. P. Boss, & S. S. Russell (Univ. of Arizona Press, Tucson), 59 (AWB2000)
André, P., Ward-Thompson, D., & Motte, F. 1996, A&A, 314, 625 (AWM96)
André, P., Motte, F., & Bacmann, A. 1999, ApJL, 513, L57 (AMB99)
Anglada, G., Estalella, R., Rodriguez, L. F., et al. 1991, ApJ, 376, 615
Anglada, G., Rodriguez, L. F., Canto, J., Estalella, R., & Torrelles, J. M. 1992, ApJ, 395, 494
Arquilla, R., & Goldsmith, P. F. 1985, ApJ, 297, 436
Bachiller, R., André, P., & Cabrit, S. 1991a, A&A, 241, L43
Bachiller, R., Martín-Pintado, J., & Planesas, P. 1991b, A&A, 251, 639
Bachiller, R., Terebey, S., Jarrett, T., et al. 1994, ApJ, 437, 296

Bacmann, A., André, P., & Puget, J.-L. 2000, A&A, 361, 555
Barsony, M., & Chandler, C. J. 1993, ApJ, 406, L71
Barsony, M., Ward-Thompson, D., André, P., & O'Linger, J. 1998, ApJ, 509, 733
Basu, S. 1997, ApJ, 485, 240
Basu, S. 1998, ApJ, 509, 229
Beckwith, S. V. W., Sargent A. I., Chini, R. S., & Güsten, R. 1990, AJ, 99, 924
Beichman, C. A., Boulanger, F., & Moshir, M. 1992, ApJ, 386, 248
Beichman, C. A., Myers, P. C., Emerson, J. P., et al. 1986, ApJ, 307, 337
Belloche, A., André, P., & Motte, F. 2001, in From Darkness to Light, ed. T. Montmerle, & P. André, in press
Benson, P. J., & Myers, P. C. 1989, ApJS, 71, 89
Bertout, C. 1989, ARA&A, 27, 351
Blottiau, P., Bouquet, S., & Chièze, J.-P. 1988, A&A, 207, 24
Bonnor, W. B. 1956, MNRAS, 116, 351
Bontemps, S., André, P., Terebey, S., & Cabrit, S. 1996, A&A, 311, 858 (BATC96)
Broguière, D., Neri, R., & Sievers, A. 1995, NIC bolometer users guide (IRAM internal report)
Butner, H. M., Evans II, N. J., Lester, D. F., Levreault, R. M., & Strom, S. E. 1991, ApJ, 376, 636
Butner, H. M., Evans II, N. J., Harvey, P. M., et al. 1990, ApJ, 364, 164
Casali, M. M. 1986, MNRAS, 223, 341
Ceccarelli, C., Hollenbach, D. J., & Tielens, A. G. G. M. 1996, ApJ, 471, 400
Cernicharo, J., Bachiller, R., & Duvert, G. 1985, A&A, 149, 273
Chandler, C. J., & Richer, J. S. 2000, ApJ, 530, 851
Chandler, C. J., Barsony, M., & Moore, T. J. T. 1998, MNRAS, 299, 789
Chen, H., Myers, P. C., Ladd, E. F., & Wood, D. O. S. 1995, ApJ, 445, 377
Chen, H., Grenfell, T. G., Myers, P. C., & Hughes, J. D. 1997, ApJ, 478, 295
Choi, M., Evans, N. J., Gregersen, E. M., & Wang, Y. 1995, ApJ, 448, 742
Ciolek, G. E., & Königl, A. 1998, ApJ, 504, 257
Ciolek, G. E., & Mouschovias, T. Ch. 1996, ApJ, 468, 749
Clemens, D. P., & Barvainis, R. 1988, ApJS, 68, 257
Contopoulos, I., Ciolek, G. E., & Königl, A. 1998, ApJ, 504, 247
Curiel, S., Raymond, J. C., Moran, J. M., Rodriguez, L. F., & Canto, J. 1990, ApJ, 365, 85
Davidson, J. A. 1987, ApJ, 315, 602
Dutrey, A., Guilloteau, S., Duvert, G., et al. 1996, A&A, 309, 493
Emerson, J. P. 1988, in Formation and Evolution of Low Mass Stars, ed. Dupree, & Lago, 21
Emerson, D. T., Klein, U., & Haslam, C. G. T. 1979, A&A, 76, 92
Evans, N. J., Rawlings, J. M. C., Shirley, Y. L., & Mundy, L. G. 2001, in preparation
Falgarone, E., & Puget, J.-L. 1985, A&A, 142, 157
Foster, P. N., & Chevalier, R. A. 1993, ApJ, 416, 303
Fuller, G. A., Ladd, E. F., & Hodapp, K. W. 1996, ApJ, 463, L97
Galli, D. 1995, Rev. Mex. A&A (Ser. de Conf.), 1, 179
Galli, D., & Shu, F. H. 1993, ApJ, 417, 220
Goldsmith, P. F., & Langer, W. D. 1978, ApJ, 222, 881
Gómez, M., Hartmann, L., Kenyon, S. J., & Hewett, R. 1993, AJ, 105, 1927
Goodman, A. A., Barranco, J. A., Wilner, D. J., & Heyer, M. H. 1998, ApJ, 504, 223
Greene, T. P, & Lada, C. J. 1996, AJ, 112, 2184
Greene, T. P., Wilking, B. A., André, P., Young, E. T., & Lada, C. J. 1994, ApJ, 434, 614
Gregersen, E. M., Evans II, N. J., Zhou, S., & Choi, M. 1997, 484, 256
Griffin, M. J., & Orton, G. S. 1993, Icarus, 105, 337
Guélin, M. 1992, in The infrared and submillimetre sky after COBE, Proceedings of the NATO Advanced Study Institute, 423
Gueth, F., Guilloteau, S., Dutrey, A., & Bachiller, R. 1997, A&A, 323, 943
Hartmann, L. W. 1998, Accretion Processes in Star Formation (Cambridge University Press), Chap. 4
Hartmann, L. W. 2000, in Star formation from the small to the large scale, ed. F. Favata, A. A. Kaas, & A. Wilson, ESA SP-445, in press [astro-ph/0001125]
Henning, Th., Michel, B., & Stognienko, R. 1995, Planet. Space Sci. (Special issue: Dust, molecules and backgrounds), 43, 1333
Henriksen, R. N., André, P., & Bontemps, S. 1997, A&A, 323, 549 (HAB97)
Heyer, M. H., Snell, R. L, Goldsmith, P. F., & Myers, P. C. 1987, ApJ, 321, 370
Hogerheijde, M. R., & Sandell, G. 2000, ApJ, 534, 880
Hogerheijde, M. R., van Dishoeck, E. F., Blake, G. A., & van Langevelde, H. J. 1997, ApJ, 489, 293
Jennings, R. E., Cameron, D. H. M., Cudlip, W., & Hirst, C. J. 1987, MNRAS, 226, 461
Keene, J., & Masson, C. R. 1990, ApJ, 355, 635
Kenyon, S. J., & Hartmann, L. W. 1995, ApJS, 101, 117
Kenyon, S. J., Calvet, N., & Hartmann, L. 1993a, ApJ, 414, 676 (KCH93)
Kenyon, S. J., Hartmann, L. W., Strom, K. M., & Strom, S. E. 1990, AJ, 99, 869 (KHSS90)
Kenyon, S. J., Whitney, B. A., Gómez, M., & Hartmann, L. 1993b, ApJ, 414, 773
Kramer, K., Alves, J., Lada, C. J., et al. 1999, A&A, 342, 257
Kreysa, E, Gemünd, H. P., Gromke, J., et al. 1998, Proc. SPIE, 3357, 319
Lada, C. J. 1987, in Star forming regions, IAU Symp. 115, ed. M. Peimbert, & J. Jugaku, 1
Ladd, E. F., Fuller, G. A., & Deane, J. R. 1998, ApJ, 495, 871
Ladd, E. F., Myers, P. C., & Goodman, A. A. 1994, ApJ, 433, 117
Ladd, E. F., Fuller, G. A., Padman, R., Myers, P. C., & Adams, F. C. 1995, ApJ, 439, 771
Ladd, E. F., Adams, F. C., Casey, S., et al. 1991, ApJ, 382, 555
Larson, R. B. 1969, MNRAS, 145, 271
Lay, O. P., Carlstrom, J. E., & Hills, R. E. 1995, ApJ, 452, L73
Lee, C. W., & Myers, P. C. 1999, ApJS, 123, 233
Li, Z.-Y. 1998, ApJ, 493, 230
Li, Z.-Y., & Shu, F. H. 1996, ApJ, 472, 211
Li, Z.-Y., & Shu, F. H. 1997, ApJ, 475, 237
Lizano, S., & Shu, F. H. 1989, ApJ, 342, 834
Looney, L. W., Mundy, L. G., & Welch, W. J. 2000, ApJ, 529, 477
Loren, R. B., Sandqvist, A. A., & Wootten, A. 1983, ApJ, 270, 620

Lucas, P. W., & Roche, P. F. 1997, MNRAS, 286, 895
Lucas, P. W., & Roche, P. F. 1998, MNRAS, 299, 699
Lynds, B. T. 1962, ApJS, 7, 1
MacLeod, J., Avery, L., Harris, A., Tacconi, L., & Shuster, K. 1994, JCMT Newsletter, 3, 46
Masunaga, H., & Inutsuka, S. 2000, ApJ, 531, 350
Masunaga, H., Miyama, S. M., & Inutsuka, S. 1998, ApJ, 495, 346
Matzner, C. D., & McKee, C. F. 2000, in press
McCaughrean, M. J., Rayner, J. T., & Zinnecker, H. 1994, ApJ, 436, L189
McLaughlin, D. E., & Pudritz, R. E. 1996, ApJ, 469, 194
McLaughlin, D. E., & Pudritz, R. E. 1997, ApJ, 476
Miroshnichenko, A., Ivezic, Z., Vinkovic, D., & Elitzur, M. 1999, ApJ, 520, 115
Motte, F., André, P., & Neri, R. 1998, A&A, 336, 150 (MAN98)
Motte, F., Gueth, F., André, P., Dutrey, A., Guilloteau, S., & Neri, R. 2001, in preparation
Mouschovias, T. Ch. 1991, in The Physics of Star Formation and Early Stellar Evolution, ed. Lada, & Kylafis, 449
Myers, P. C. 1987, in Star forming regions, IAU Symp. 115, ed. M. Peimbert, & J. Jugaku, 33
Myers, P. C. 1998, ApJL, 496, L109
Myers, P. C., & Benson, P. J. 1983, ApJ, 266, 309
Myers, P. C., & Fuller, G. 1992, ApJ, 396, 631
Myers, P. C., & Ladd, E. F. 1993, ApJ, 413, L47
Myers, P. C., Fuller, G. A., Mathieu, R. D., et al. 1987, ApJ, 319, 340 (M 87)
Myers, P. C., Adams, F. C., Chen, H., & Schaff, E. 1998, ApJ, 492, 703
Mundt, R., Brugel, E. W., & Bührke, T. 1987, ApJ, 319, 275
Neufeld, D. A., Lepp, S., & Melnick, G. J. 1995, ApJS, 100, 132
Ohashi, N., Hayashi, M., Kawabe, R., & Ishiguro, M. 1996, ApJ, 466, 317
Ohashi, N., Kawabe, R., Hayashi, M., & Ishiguro, M. 1991, AJ, 102, 2054
Ossenkopf, V., & Henning, Th. 1994, A&A, 291, 943
Padgett, D. L., Brandner, W., Stapelfeldt, et al. 1999, AJ, 117, 1490
Parker, N. D. 1988, MNRAS, 235, 139
Penston, R. B. 1969, MNRAS, 144, 425
Reipurth, B., Chini, R., Krügel, E., Kreysa, E., & Sievers, A. 1993, A&A, 273, 221
Safier, P. N., McKee, C. F., & Stahler, S. W. 1997, ApJ, 485, 660
Sandell, G., Aspin, C., Duncan, W. D., Russell, A. P. G., & Robson, E. I. 1991, ApJ, 376, L17
Sandell, G., Knee, L. B. G., Aspin, C., Robson, I. E., & Russell, A. P. G. 1994, A&A, 285, L1
Saraceno, P., André, P., Ceccarelli, C., Griffin, M., & Molinari, S. 1996, A&A, 309, 827
Sonnhalter, C., Preibisch, Th., & Yorke, H. W. 1995, A&A, 299, 545
Shirley, Y., Evans II, N. J., Rawlings, J. M. C., & Gregersen, E. M. 2000, in press
Shu, F. H. 1977, ApJ, 214, 488
Shu, F. H., Adams, F. C., & Lizano, S. 1987, ARA&A, 25, 23
Shu, F. H., Shang, H., & Lee, T. 1996, Sci, 271, 1545
Stahler, S. W. 1988, ApJ, 332, 804
Tamura, M., Gatley, I., Waller, W., & Werner, M. W. 1991, ApJL, 374, L25
Terebey, S., Chandler, C. J., & André, P. 1993, ApJ, 414, 759
Terebey, S., Shu, F. H., & Cassen, P. C. 1984, ApJ, 286, 529
Terebey, S., Vogel, S. N., & Myers, P. C. 1992, ApJ, 390, 181
Terquem, C., Bertout, C. 1993, A&A, 274, 291
Terquem, C., Bertout, C. 1996, MNRAS, 279, 415
Tomisaka, K. 1996, PASJ, 48, L97
Umemoto, T., Iwata, T., Fukui, Y., et al. 1992, ApJ, 392, L83
Walker, C. K., Adams, F. C., & Lada, C. J. 1990, ApJ, 349, 515
Ward-Thompson, D., Motte, F., & André, P. 1999, MNRAS, 305, 143
Ward-Thompson, D., Scott, P. F., Hills, R. E., & André, P. 1994, MNRAS, 268, 276
Whitworth, A., & Summers, D. 1985, MNRAS, 214, 1
Wilking, B. A., Lada, C. J., & Young, E. T. 1989, ApJ, 340, 823
Yun, J. L., & Clemens, D. P. 1991, ApJ, 381, 474 (YC91)
Yun, J. L., & Clemens, D. P. 1992, ApJ, 385, L21